



CERN-EP-2023-054

22 March 2023

Measurements of inclusive J/ψ production at midrapidity and forward rapidity in Pb–Pb collisions at $\sqrt{s_{NN}} = 5.02$ TeV

ALICE Collaboration*

Abstract

The measurements of the inclusive J/ψ yield at midrapidity ($|y| < 0.9$) and forward rapidity ($2.5 < y < 4$) in Pb–Pb collisions at $\sqrt{s_{NN}} = 5.02$ TeV with the ALICE detector at the LHC are reported. The inclusive J/ψ production yields and nuclear modification factors, R_{AA} , are measured as a function of the collision centrality, J/ψ transverse momentum (p_T), and rapidity. The J/ψ average transverse momentum and squared transverse momentum ($\langle p_T \rangle$ and $\langle p_T^2 \rangle$) are evaluated as a function of the centrality at midrapidity. Compared to the previous ALICE publications, here the entire Pb–Pb collisions dataset collected during the LHC Run 2 is used, which improves the precision of the measurements and extends the p_T coverage. The p_T -integrated R_{AA} shows a hint of an increasing trend towards unity from semicentral to central collisions at midrapidity, while it is flat at forward rapidity. The p_T -differential R_{AA} shows a strong suppression at high p_T with less suppression at low p_T where it reaches a larger value at midrapidity compared to forward rapidity. The ratio of the p_T -integrated yields of J/ψ to those of D^0 mesons is reported for the first time for the central and semicentral event classes at midrapidity. Model calculations implementing charmonium production via the coalescence of charm quarks and antiquarks during the fireball evolution (transport models) or in a statistical approach with thermal weights are in good agreement with the data at low p_T . At higher p_T , the data are well described by transport models and a model based on energy loss in the strongly-interacting medium produced in nuclear collisions at the LHC.

1 Introduction

Quantum chromodynamics (QCD) is the theory describing the strong interaction. Lattice QCD, i.e. the discrete formulation of QCD, predicts the existence of a state of deconfined matter at high energy density that is characterised by quark and gluon degrees of freedom [1, 2]. This quark–gluon plasma (QGP) is created during the early hot and dense stage of heavy-ion collisions at ultra-relativistic energies.

The heavy quarks, charm (c) and beauty (b), are unique probes for this phase of matter [3, 4]. Due to their large masses, they are produced as quark–antiquark pairs in hard partonic scattering processes in the early stage of the collision, and they thus experience the full evolution of the system. While the majority of the produced heavy quarks and antiquarks hadronise independently into open heavy-flavour hadrons, bound quarkonium states can also be formed [5]. However, it has been predicted that the formation of bound states should be suppressed due to the mechanism of colour screening where the large density of colour charges in the QGP hinders the production of bound quarkonia [6, 7]. The degree of suppression of the various quarkonium states depends on their binding energy along with the medium properties, such as its temperature. Consequently, the measurements of quarkonium production rates in heavy-ion collisions have been considered as a potential thermometer of the medium.

The production of J/ψ , the charmonium ground state with quantum numbers $J^{PC} = 1^{--}$, has been studied extensively in heavy-ion collisions over the last several decades. Suppression of the J/ψ yield was observed in nucleus–nucleus collisions with respect to the expectation from proton–proton collisions at the SPS (up to centre-of-mass energy per nucleon pair $\sqrt{s_{NN}} = 17$ GeV) [8–10], at RHIC ($\sqrt{s_{NN}}$ up to 200 GeV) [11–14] and at the LHC ($\sqrt{s_{NN}} = 2.76$ TeV [15–18] and 5.02 TeV [19–24]). However, contrary to the prediction from the colour-screening scenario, the measured suppression does not increase with increasing collision energy from RHIC to LHC despite of an increased energy density of the produced QGP. At LHC energies, J/ψ production is found to be less suppressed than at the lower RHIC energies, in particular at low transverse momentum, p_T , of the J/ψ [18, 25–27]. In addition, a significant azimuthal anisotropy in the J/ψ production was observed via the elliptic and triangular flow measurements reported in Refs. [28, 29]. These observations are explained by an additional J/ψ production mechanism, referred to as (re)generation in the following, in which copiously produced uncorrelated charm quarks and antiquarks bind into J/ψ mesons [30, 31]. This process can only take place in a deconfined medium, and its contribution to the measured J/ψ yield increases with the density of $c\bar{c}$ pairs and, therefore, with increasing collision energy and decreasing p_T [32–34]. With increasing p_T , (re)generation becomes less relevant for J/ψ production and, instead, charmonium dissociation and the fragmentation of high-energy partons into charmonia become dominant. In the latter case, the suppression of high- p_T J/ψ yields should reflect the energy loss of partons [35], which is mostly of radiative nature in this kinematic regime.

The formation process of charmonia in heavy-ion collisions is complex and various phenomenological approaches are considered. In the statistical hadronization scenario, the relative abundances of charmonium states with respect to other charmed hadrons are determined by thermal weights [30, 32] at the system chemical freeze-out. In microscopic transport and comover interaction models, charmonia are continuously produced and broken up during their propagation through the QGP [31, 33, 34, 36]. Furthermore, it is important to consider cold nuclear matter (CNM) effects. In particular, the modification of the parton distribution functions in nuclei with respect to nucleons [37] has to be taken into account for the interpretation of the results. These CNM effects were investigated in ALICE especially with proton–nucleus collisions [38–44].

For a better assessment of the production mechanisms, systematic measurements of the centrality, p_T , and rapidity dependence of J/ψ production are pivotal. In this article, the ALICE results on inclusive J/ψ production at midrapidity ($|y| < 0.9$) for $0.15 < p_T < 15$ GeV/c and forward rapidity ($2.5 < y < 4$) for $0.3 < p_T < 20$ GeV/c, from the full Run 2 data sample at the LHC, are reported. Inclusive J/ψ

measurements contain a prompt J/ψ contribution from direct J/ψ and decay from heavier charmonium states, and a non-prompt J/ψ contribution from the decay of beauty hadrons. The precision of the measurements, using the entire Run 2 data sample, improved significantly compared to previous ones [20, 21] and the measurements could be extended up to 15 GeV/c and 20 GeV/c at mid and forward rapidity, respectively. The p_T -differential J/ψ yields in Pb–Pb collisions at $\sqrt{s_{NN}} = 5.02$ TeV are measured in various centrality classes. At midrapidity, the average transverse momentum $\langle p_T \rangle$ as well as squared transverse momentum $\langle p_T^2 \rangle$ are determined, which provide a quantitative estimation of the evolution of the p_T spectra as a function of centrality. The nuclear modification factor R_{AA} defined, as the ratio of the yield in Pb–Pb to the corresponding yield in pp collisions scaled by the number of binary nucleon–nucleon collisions is calculated. The results as a function of p_T and collision centrality are compared with model calculations employing the statistical hadronisation [32], microscopic parton transport [33, 34], comover [36], and energy loss [35] approaches.

2 Apparatus and data sample

A complete description of the ALICE apparatus and its performance is given in Refs. [45, 46]. The central barrel detectors, for the dielectron analysis, and the muon spectrometer, for the dimuon analysis, covering midrapidity and forward rapidity, respectively, were used in the analyses reported in this paper.

At midrapidity, the main detectors employed in the analysis are the Time Projection Chamber (TPC) [47] and the Inner Tracking System (ITS) [48], both immersed in a uniform magnetic field of 0.5 T provided by a solenoid magnet. The TPC is used for tracking and particle identification. It covers the pseudorapidity range $|\eta| < 0.9$ for tracks with full radial length and has full coverage in azimuth. It provides excellent momentum resolution and electron–hadron separation in a wide range of track transverse momentum. The ITS is a cylindrical six-layer silicon detector, with the innermost layer located at 3.9 cm from the beam pipe, providing additional space points for tracking that enhance the spatial resolution in the reconstruction of primary and secondary vertices.

At forward rapidity, the muon spectrometer [49, 50] detects muons in the range $-4 < \eta < -2.5$. It consists of a 3 Tm dipole associated with a tracking and a trigger system. A front absorber with a thickness of 10 interaction lengths is placed before the tracking system in order to filter out hadrons produced in the interaction. The tracking system consists of five tracking stations, each one made of two planes of cathode pad chambers. An iron wall with 7.2 interaction length thickness is located between the tracking and trigger stations in order to stop secondary hadrons escaping the front absorber and low momentum muons produced predominantly from π and K decays. The trigger system consists of two stations, each one made of two planes of resistive plate chambers. Finally, a conical absorber around the beam pipe protects the spectrometer against secondary particles produced by the interaction of primary particles with large pseudorapidity at the beam pipe. In the analysis at forward rapidity, the determination of the primary vertex of the collision is provided by the Silicon Pixel Detector (SPD) that constitutes the two innermost layers of the ITS.

Both analyses, at midrapidity and forward rapidity, use the V0 [51] and Zero Degree Calorimeter (ZDC) [52] detectors. The V0 detector consists of two scintillator detector arrays and covers the full azimuth in the pseudorapidity regions $-3.7 < \eta < -1.7$ and $2.8 < \eta < 5.1$, respectively. It is used for triggering, beam–gas background rejection, and characterisation of the event centrality. The ZDC detectors are located at a distance of 112.5 m on both sides of the interaction region along the beam direction, and they detect spectator nucleons emitted at zero degree with respect to the LHC beam axis. They are used to reject electromagnetic Pb–Pb interactions.

The trigger for minimum-bias (MB) events was provided by the coincidence of signals in the two scintillator arrays of the V0 detector. The dimuon analysis relies on a dimuon trigger which requires, in addition to the MB trigger, the detection of two opposite-sign tracks in the muon trigger system. The muon trigger

selects muon candidates with a p_{T} larger than a threshold of ~ 1 GeV/ c . The trigger efficiency reaches 50% at this threshold value and a plateau value of 98% at $p_{\text{T}} \sim 2.5$ GeV/ c [53].

The results presented in this article are based on the data sample collected by ALICE from Pb–Pb collisions at $\sqrt{s_{\text{NN}}} = 5.02$ TeV in 2015 and 2018 during Run 2 at the LHC. During the 2018 data taking, the Pb–Pb dataset for the central barrel was enhanced with central (0–10%) and semicentral (30–50%) events. In total, the integrated luminosity corresponding to the analysed data sample was about $105 \mu\text{b}^{-1}$ and $51 \mu\text{b}^{-1}$ for the central and semicentral events, respectively. For the other centrality intervals, the integrated luminosity of the data sample was $22 \mu\text{b}^{-1}$. For the analysis at forward rapidity, the dimuon triggered sample corresponds to an integrated luminosity of $756 \mu\text{b}^{-1}$. At midrapidity, triggered events containing collisions that overlap within a time window smaller than the readout time of the TPC were removed to preserve a uniform particle identification performance of the TPC, which is sensitive to the total charge produced by the ionising tracks in the sensitive volume. Only events with the primary vertex, reconstructed within ± 10 cm from the nominal interaction point in the beam direction, were considered for further analysis at midrapidity. In the forward analysis, there was no selection on the primary vertex.

3 Analysis details

The primary observable is the p_{T} -differential J/ψ yield per unit of rapidity $d^2N/(dy dp_{\text{T}})$. For a given interval of centrality, rapidity (Δy), and transverse momentum (Δp_{T}), this is obtained as

$$\frac{d^2N}{dy dp_{\text{T}}} = \frac{N_{\text{J}/\psi}}{N_{\text{ev}} \times \text{BR}_{\text{J}/\psi \rightarrow l^+l^-} \times (A \times \varepsilon) \times \Delta y \times \Delta p_{\text{T}}}, \quad (1)$$

where $N_{\text{J}/\psi}$ is the number of reconstructed J/ψ mesons, N_{ev} is the number of events corresponding to the analysed centrality interval, and $(A \times \varepsilon)$ is the acceptance times efficiency factor. The branching ratio (BR) corresponds to either the dielectron or the dimuon J/ψ decay channel. Since the analysis at forward rapidity was based on a sample of dimuon-triggered events, the equivalent N_{ev} was obtained as the product of the number of dimuon-triggered events times the inverse of the probability of having a dimuon trigger in a MB triggered event, F_{norm} [40, 54]. The number of equivalent N_{ev} was first obtained for the 0–90% centrality class and was then scaled to the centrality classes considered in the analysis.

The nuclear modification factor, R_{AA} , is obtained as

$$R_{\text{AA}} = \frac{d^2N/(dy dp_{\text{T}})}{\langle T_{\text{AA}} \rangle d^2\sigma_{\text{pp}}/(dy dp_{\text{T}})}, \quad (2)$$

where $\langle T_{\text{AA}} \rangle$ is the average nuclear overlap function as described in Ref. [55] and given in Table 1 for the centrality intervals used for the analyses at midrapidity and forward rapidity. The R_{AA} is evaluated as a function of the average number of participant nucleons, N_{part} , corresponding to a given centrality class (as shown in Table 1), and as a function of the J/ψ p_{T} . The differential J/ψ production cross section in pp collisions, $d^2\sigma_{\text{pp}}/(dy dp_{\text{T}})$, was measured at both midrapidity and forward rapidity as reported in Refs. [56] and [57], respectively. At midrapidity, the statistics do not allow to obtain the cross section for $p_{\text{T}} > 10$ GeV/ c and an extrapolation is applied for the last p_{T} interval ($10 < p_{\text{T}} < 15$ GeV/ c). The details of this approach are described in Ref. [58, 59].

The p_{T} -differential J/ψ yields at midrapidity were studied further by extracting the $\langle p_{\text{T}} \rangle$ and $\langle p_{\text{T}}^2 \rangle$ in fine centrality intervals, as described later in this section. For quantitative comparisons of the p_{T} distributions, the ratio r_{AA} of the J/ψ $\langle p_{\text{T}}^2 \rangle$ measured in Pb–Pb collisions to the one obtained in pp collisions at the same energy is calculated as

$$r_{\text{AA}} = \frac{\langle p_{\text{T}}^2 \rangle_{\text{PbPb}}}{\langle p_{\text{T}}^2 \rangle_{\text{pp}}}. \quad (3)$$

Table 1: Average nuclear overlap function $\langle T_{AA} \rangle$ and the average number of participants $\langle N_{part} \rangle$ in Pb–Pb collisions at $\sqrt{s_{NN}} = 5.02$ TeV for the centrality classes used in the analyses at midrapidity (upper) and forward rapidity (lower).

Centrality	$\langle T_{AA} \rangle$ (1/mb)	$\langle N_{part} \rangle$
0–5%	26.08 ± 0.18	383.40 ± 0.57
5–10%	20.44 ± 0.17	331.20 ± 1.03
10–20%	14.4 ± 0.13	262.00 ± 1.15
20–30%	8.77 ± 0.10	187.90 ± 1.34
30–40%	5.09 ± 0.08	130.80 ± 1.33
40–50%	2.75 ± 0.05	87.14 ± 0.93
50–70%	0.98 ± 0.02	42.65 ± 0.69
70–90%	0.16 ± 0.004	11.34 ± 0.16
0–20%	18.83 ± 0.14	309.7 ± 0.89
20–40%	6.93 ± 0.09	159.4 ± 1.32
40–90%	1.00 ± 0.02	39.03 ± 0.53

3.1 J/ψ raw yield extraction

The J/ψ mesons are reconstructed employing the e^+e^- decay channel at midrapidity and the $\mu^+\mu^-$ decay channel at forward rapidity. The analysis techniques are discussed in detail in Refs. [18, 20, 21]. Here, only a brief overview is given and differences with respect to previous analyses are highlighted.

Electron candidates for the analysis at midrapidity are tracks reconstructed in both the ITS and TPC in the pseudorapidity range $|\eta| < 0.9$ and with a $p_T > 1$ GeV/ c to suppress combinatorial background. All tracks are required to have at least one hit in the SPD layers and at least 70 out of a maximum of 159 clusters reconstructed in the TPC. These and other quality criteria that were applied in addition (see Ref. [20]) ensure good tracking resolution and particle identification. They reduce the background electrons from the conversion of photons in the detector material or from long lived weakly-decaying hadrons as well as tracks from pileup collisions, occurring within the readout time of the TPC. Electrons and positrons are identified using selections on the specific energy loss, dE/dx , in the TPC gaseous volume. The measured dE/dx is required to be within 3 standard deviations (σ) relative to the expected electron specific energy loss corresponding to the track momentum, and more than 3.5σ different from either the π or proton specific energy loss hypotheses. Electrons from photon conversions surviving the track quality criteria are rejected using a technique where candidate electrons are paired with other electrons selected with less strict criteria to enhance the probability of finding the conversion partner, as described in detail in Ref. [21].

Muon candidates were selected such that the track pseudorapidity is within the geometrical acceptance of the muon spectrometer, $-4 < \eta < -2.5$, and that the reconstructed track matches a track segment reconstructed in the trigger system. The transverse position of the tracks at the end of the absorber is required to be $17.6 < R_{abs} < 89.5$ cm in order to reject tracks crossing the thickest part of the absorber. In addition, a selection was applied on the product of the track momentum and the transverse distance to the primary vertex in order to reduce the contamination produced by particles that do not originate from the interaction point.

The number of reconstructed J/ψ mesons, i.e. the raw J/ψ yield, was obtained by constructing the invariant-mass distribution of all the possible opposite-sign dileptons with rapidity selections of $2.5 < y < 4$ for dimuons and $|y| < 0.9$ for dielectrons. At midrapidity, the signal extraction was performed in two steps. First, the combinatorial background was estimated using an event-mixing technique [21] and subtracted from the invariant-mass distribution. In the second step, the remaining distribution was fitted with a two-component function, one corresponding to the J/ψ signal and the other to the residual

background, which mainly arises from correlated semileptonic decays of heavy-flavour hadrons. The J/ψ signal line shape was obtained from Monte Carlo (MC) simulations of J/ψ mesons decaying in the dielectron channel embedded in simulated Pb–Pb collisions, as described below, while for the residual background a second-order polynomial function was employed. The raw J/ψ yield was obtained by first counting the dielectron pairs in the mass range $2.92 < m_{e^+e^-} < 3.16$ GeV/ c^2 in the combinatorial-background subtracted invariant-mass distribution, and then subtracting the residual background based on a two-component fit. Finally, the raw J/ψ -meson yield is corrected for the fraction of J/ψ reconstructed outside of the counting mass interval, as described in more detail in Section 3.3. This procedure is illustrated in the left panels of Fig. 1 for the collision centrality interval 0–5% and $p_T > 0.15$ GeV/ c . The upper left panel shows the invariant-mass distributions for the opposite-sign dielectrons constructed from the same event (black) and mixed events (red). The fitting procedure of the combinatorial background subtracted invariant-mass distribution discussed above is illustrated in the lower left panel.

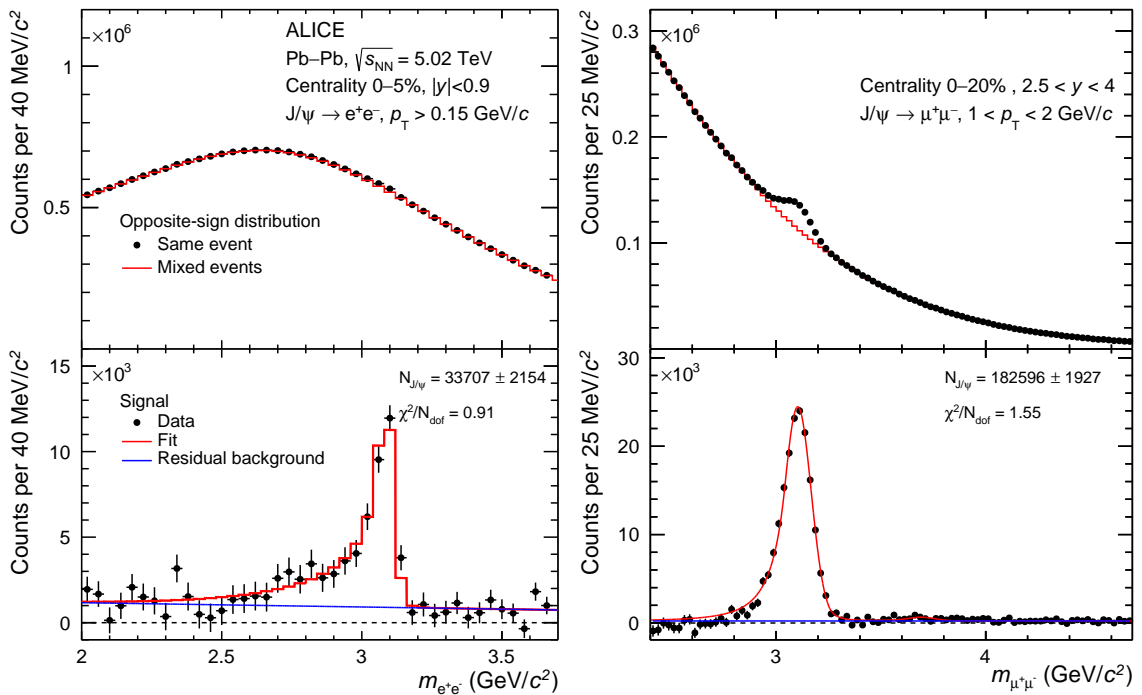


Figure 1: Upper panels: invariant-mass distribution of opposite-sign lepton pairs from the same event (black points) and mixed events (red histograms) at midrapidity (left) and forward rapidity (right) in Pb–Pb collisions at $\sqrt{s_{NN}} = 5.02$ TeV. Lower panels: invariant-mass distribution after the background subtraction with the event-mixing technique. The fit curves, shown in red, represent the sum of the signal and background shapes and the blue curves correspond to the residual background.

At forward rapidity, two different methods were used to extract the number of J/ψ counts. In the first method, the invariant-mass distributions were fitted with a sum of a signal and a background function, while in the second method the event-mixing technique was employed, as described in Ref. [18]. The fit functions corresponding to the signal are either a double-sided Crystal Ball function (CB2) or a pseudo-Gaussian with a mass-dependent width [60]. In both cases, the J/ψ pole mass and width were free parameters of the fit, while the non-Gaussian tail parameters were fixed. Two sets of tail parameters were obtained, one based on MC simulations and one extracted from a large data sample of pp collisions at $\sqrt{s} = 13$ TeV [61]. The MC simulations were embedded into real MB events in order to properly account for the effect of the detector occupancy. The $\psi(2S)$ resonance was also included in the fit to the invariant-mass spectrum, using the same signal function as for the J/ψ with mass and width bound to those of the J/ψ [61, 62]. The background functions employed in the first method were either a variable-width

Gaussian [60] or a ratio of a second order to a third order polynomial. The residual background in the second method was parameterised with a sum of two exponential functions. Finally, two invariant-mass ranges were considered for the fit procedure: $2.2 < m_{\mu^+\mu^-} < 4.5$ and $2.4 < m_{\mu^+\mu^-} < 4.7$ GeV/c^2 . An example of the signal extraction fit is shown in the right panel of Fig. 1 before (upper plot) and after (lower plot) the subtraction of the combinatorial background estimated with the event-mixing technique. For each p_{T} and centrality interval, several fits were performed with the two different approaches, different combinations of signal and background functions, signal tail parameters, and fitting ranges. The number of J/ψ was obtained as the average of the results from the various fitting methods [57]. These various fitting methods are used to determine the systematic uncertainties on the yield extraction as described in Section 3.4.

About 9.0×10^5 and 8.2×10^4 raw J/ψ counts are measured at forward rapidity and midrapidity, respectively, integrated over all available centrality and p_{T} intervals.

3.2 J/ψ $\langle p_{\text{T}} \rangle$ and $\langle p_{\text{T}}^2 \rangle$ extraction

At midrapidity, a quantitative study of the J/ψ p_{T} spectrum in fine centrality intervals is conducted by extracting the J/ψ mean p_{T} , $\langle p_{\text{T}} \rangle_{J/\psi}$, and mean p_{T} squared, $\langle p_{\text{T}}^2 \rangle_{J/\psi}$. For a given centrality interval, these quantities are obtained based on a fit to the mass dependent $\langle p_{\text{T}} \rangle$ and $\langle p_{\text{T}}^2 \rangle$ distributions after efficiency correction, using a function defined as:

$$X(m_{e^+e^-}) = f(m_{e^+e^-}) \times X_{J/\psi} + (1 - f(m_{e^+e^-})) \times X_{\text{bkg}}(m_{e^+e^-}) \quad (4)$$

where X stands for either the $\langle p_{\text{T}} \rangle$ or $\langle p_{\text{T}}^2 \rangle$, and f is the invariant-mass dependent fraction of J/ψ signal determined in the signal-extraction procedure explained above. The invariant-mass dependent background component $X_{\text{bkg}}(m_{e^+e^-})$ is determined from the event-mixing procedure plus a second order polynomial function for the residual background. Examples of these fits for the $\langle p_{\text{T}} \rangle$ observable are shown in Fig. 2.

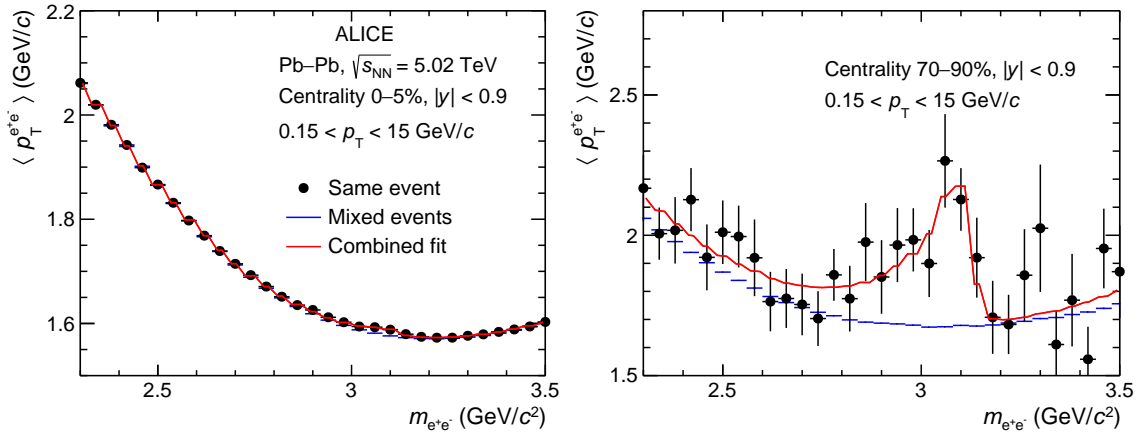


Figure 2: J/ψ $\langle p_{\text{T}} \rangle$ extraction in Pb–Pb collisions at $\sqrt{s_{\text{NN}}} = 5.02$ TeV at midrapidity for the 0–5% (left panel) and the 70–90% (right panel) centrality interval. The data points correspond to opposite-sign e^+e^- pairs from the same event, the blue line to the e^+e^- pairs from mixed events, and the red line is the combined fit that includes the mixed events and residual background which is described by the polynomial function.

3.3 Acceptance and efficiency correction

The acceptance times reconstruction efficiency factor ($A \times \varepsilon$), which enters into Eq. 1, was computed employing both MC and data-driven methods. At midrapidity, this factor includes the kinematic ac-

ceptance, track-reconstruction and particle-identification efficiencies, and the fraction of J/ψ with an invariant mass in the signal counting range. With the exception of the particle identification, obtained with a data-driven method, the corrections were obtained using a MC simulation of J/ψ embedded in simulated Pb–Pb collisions. The Pb–Pb collisions were generated using the HIJING 1.0 model [63], while the J/ψ were generated using a cocktail of prompt J/ψ with a kinematic distribution tuned to existing measurements and non-prompt J/ψ from beauty hadrons forced to decay into channels containing J/ψ , using PYTHIA 6.4 [64]. The e^+e^- decay of the embedded J/ψ was handled using PHOTOS [65]. Both the prompt J/ψ and the beauty hadrons forced to decay into non-prompt J/ψ were assumed to be unpolarised, in agreement with existing measurements, which indicate small or no polarisation [66, 67]. All generated particles were transported through the ALICE detector setup using GEANT3 [68], taking into account the time dependence of detector conditions during the 2015 and 2018 data-taking periods. For the determination of the particle-identification efficiency, a clean sample of electrons from photon conversions, passing similar quality selection criteria as primary electrons in the TPC, is used to compute differential maps in pseudorapidity, azimuthal angle φ and momentum p for the single-electron selection efficiency. These were then propagated to the J/ψ dielectron pairs using the phase-space distribution of the J/ψ decay simulated in the above mentioned MC simulations. The total $(A \times \epsilon)$ for the p_T -integrated J/ψ yields is about 6.5% in the 0–10% centrality interval, and it slightly increases towards more peripheral collisions. As a function of p_T , the $(A \times \epsilon)$ has a non-monotonic behaviour, with a minimum value of 5.6% around $p_T = 2$ GeV/c, and a maximum of about 9% towards zero and high p_T .

At forward rapidity, the acceptance and reconstruction efficiency values were determined using simulated J/ψ mesons forced to decay via the dimuon channel, embedded into real events. The J/ψ p_T - and y -differential distributions used in the simulation were adjusted to measurements via an iterative procedure, and separately for all centrality intervals employed in this analysis. The J/ψ were assumed to be unpolarised, in agreement with the small polarisation, compatible with zero, measured in Pb–Pb collisions for $2 < p_T < 10$ GeV/c [67]. As in the analysis at midrapidity, the simulations take into account the time dependence of the detector conditions, such as the status of the tracking chambers and the residual detector element misalignment. The trigger-chamber efficiency was determined from data and used as input in the simulations. The $(A \times \epsilon)$ reaches a minimum of 11% at $p_T \approx 2$ GeV/c and increases up to 13% at low p_T and up to 46% at high p_T in the 0–20% centrality interval. It increases slightly towards peripheral collisions [46].

3.4 Systematic uncertainties

The considered sources of systematic uncertainty for the analysis at midrapidity include central-barrel tracking, electron identification, signal extraction, and the kinematics of the J/ψ injected in the MC simulations. For the analysis at forward rapidity, the main systematic uncertainties originate from the signal extraction, the muon tracking and trigger efficiencies, and the kinematics of the J/ψ used in the embedded MC simulations. In addition, for the R_{AA} , uncertainties on the pp reference and the nuclear overlap function are included in both analyses [55]. The uncertainty on the J/ψ decay branching ratio and the evaluated systematic uncertainties are summarised in Table 2 and Table 3 for the analysis at midrapidity and forward rapidity, respectively.

At midrapidity, the tracking uncertainty is the largest source of systematic uncertainty and it is dominated by the ITS–TPC track matching. This was determined based on the difference in the matching efficiency observed for single tracks between data and MC simulations. The systematic uncertainty due to the electron identification takes into account the residual miscalibration of the TPC particle identification (PID) response and also the statistical uncertainty of the clean electron sample used to compute the identification efficiency. For its estimation, the PID selection criteria (both electron inclusion and hadron rejection) are varied, each time obtaining a new set of raw yields and corresponding PID efficiencies. The assigned systematic uncertainty is taken as the standard deviation of the distribution of the corrected results obtained in this procedure. The systematic uncertainty of the signal extraction includes

one component from the J/ψ signal shape obtained from MC simulations and one component related to the description of the dielectron background. The former was determined by varying the mass range in which the signal is counted and recomputing each time the corresponding signal fraction correction, while the latter was determined by repeating the fit to the invariant-mass distribution in different mass ranges. The standard deviation of the corrected yield distribution was then taken as the systematic uncertainty. Since the J/ψ efficiency depends on p_T , the average efficiency computed over wide p_T intervals depends in turn on the underlying J/ψ p_T distribution used in the MC simulations. The corresponding uncertainty was minimised by iteratively tuning the injected p_T spectrum to match the corrected spectrum measured in this analysis. A systematic uncertainty which takes into account possible variations of the p_T spectrum, statistically compatible with the finally measured p_T spectrum, was assigned and it is typically below 1%. The total systematic uncertainty on the J/ψ corrected yield varies in the range 6–10% in different p_T and centrality intervals. The systematic uncertainties, which are dominated by the tracking uncertainties, are correlated over centrality and p_T to a very large extent. The systematic uncertainties for $\langle p_T \rangle$ and $\langle p_T^2 \rangle$ are evaluated via similar procedures as for the p_T integrated yields. The uncertainties from signal extraction and track selection criteria range, respectively, from 0.2 to 1.2% and from 0.5 to 1.3%. The electron identification and ITS–TPC matching systematic uncertainties are calculated by propagating the p_T -differential systematic uncertainties to the $\langle p_T \rangle$ based on the measured p_T -differential spectrum.

In the analysis at forward rapidity, the systematic uncertainty corresponding to the signal extraction was determined using several variations of the fit to the invariant-mass spectra, including the fit method, the signal and background functions, and the fitted mass range. This uncertainty varies in the range 1.5–10.7% depending on the p_T interval and centrality class. The systematic uncertainty on $(A \times \epsilon)$ depends on the uncertainty on the p_T and y distributions of the simulated J/ψ , and on the tracking, trigger, and matching efficiency. The first two were evaluated by varying the p_T and y spectrum for each centrality interval, taking into account the correlations between the p_T and y distributions. The systematic uncertainty was estimated as the largest difference between the nominal $(A \times \epsilon)$ and the one estimated from the variations. It ranges between 0.2% and 4.1%. The systematic uncertainty on the muon tracking efficiency was estimated based on the difference between the single-muon tracking efficiency obtained in data and MC with a method that uses the redundancy of the tracking information in each station. The corresponding uncertainty for dimuons was evaluated to be 3% and constant over p_T . An additional systematic uncertainty is ascribed to the loss of tracking efficiency due to occupancy effects in the most central events and was estimated to range between 0.5 and 1%, increasing towards more central events. The systematic uncertainty on the trigger efficiency has two components, one due to the intrinsic efficiency of the trigger chambers and another one due to the trigger response. The first component was estimated from the uncertainties on the single-muon trigger efficiency measured from data and used in the simulations. The second component was evaluated by comparing the p_T dependence of the trigger response function of the single muon between data and MC. The two sources were added in quadrature and the obtained uncertainty ranges between 1.5 and 2%. Finally, a 1% systematic uncertainty is assigned, related to the choice of the χ^2 selection used to define the matching between the tracks reconstructed in the tracking system and the track segments reconstructed in the trigger system. The uncertainty on F_{norm} was estimated by using two methods. First, the opposite-sign dimuon trigger condition was applied when analysing recorded MB events and, second, the counting rate of the dimuon and MB triggers were compared. The estimated uncertainty on F_{norm} was obtained by comparing the two methods and it amounts to 0.7%.

The systematic uncertainties on $\langle T_{AA} \rangle$ were obtained as described in Ref. [55] and the values are listed in Table 1 for both analyses, at midrapidity and forward rapidity. The systematic uncertainty on the definition of the centrality interval was estimated using variations of $\pm 1\%$ of the V0 signal amplitude corresponding to 90% of the hadronic Pb–Pb cross section and redefining correspondingly the centrality intervals. The systematic uncertainty of the centrality limit depends on the width of the centrality classes

and it ranges from 1 to 6% and from 0 to 2.8%, as shown in Tables 2 and 3 for the analyses at midrapidity and forward rapidity, respectively.

The systematic uncertainties on the J/ψ reference cross section in pp collisions at $\sqrt{s} = 5.02$ TeV as obtained in Refs. [57, 69] are provided in Table 2 and Table 3. The correlations of the systematic uncertainties over centrality and p_T depend on the mid and forward rapidity analysis and they are indicated in Table 2 and 3.

Table 2: Systematic uncertainties on the p_T -integrated ($0.15 < p_T < 15$ GeV/c) measurement at midrapidity for different centrality intervals. The individual contributions and the total uncertainties are given in percentage. It is considered that all the uncertainties are correlated over centrality and p_T to a very large extent.

Centrality (%)	0–5	5–10	10–20	20–30	30–40	40–50	50–70	70–90
Signal extraction	2.5	2.7	1.9	6.6	2.5	1.0	1.8	2.5
MC input	0.5	0.5	0.5	0.5	0.5	0.5	0.5	0.5
Tracking	10.1	10.1	8.5	8.5	8.0	8.0	7.9	7.9
PID	1.6	1.3	1.4	1.4	1.1	1.2	1.1	1.3
Centrality limit	1.0	1.0	1.0	1.0	1.0	1.0	5.7	6.0
Total	10.6	10.5	8.8	10.8	9.0	8.2	10.0	10.3
T_{AA} (only on R_{AA})	0.7	0.8	0.9	1.2	1.6	1.7	2.0	2.3
pp reference (only on R_{AA})					5.8			
Branching ratio (only on yield)					0.5			

Table 3: Systematic uncertainties on the p_T -differential measurement at forward rapidity for various centrality intervals. The individual contributions are given in percentage. When a range is given, it corresponds to the minimum and maximum values obtained in the p_T interval. Values marked with an asterisk correspond to the uncertainties correlated over p_T .

Centrality (%)	0–20%	20–40%	40–90%
F_{norm}		0.7*	
Signal extraction	1.5–5.8	1.9–4.5	1.6–10.7
MC input	1.8–4.1	0.2–2.1	0.9–1.8
Tracking efficiency	3.0 + 1.0*	3.0 + 0.5*	3.0
Trigger efficiency	1.5–2.0 + 1.0*	1.5–2.0 + 0.5*	1.5–2.0
Matching efficiency	1.0	1.0	1.0
Centrality limit	–	0.8*	2.8*
T_{AA} (only on R_{AA})	0.8*	1.3*	2.0*
pp reference (only on R_{AA})		3.5–5.6 + 1.9*	
Branching ratio (only on yield)		0.5*	

4 Results

4.1 Inclusive J/ψ yields

The fully corrected inclusive J/ψ p_T -differential yields, $d^2N/(dydp_T)$, were obtained according to Eq. 1 in centrality intervals in Pb–Pb collisions at $\sqrt{s_{NN}} = 5.02$ TeV at midrapidity ($|y| < 0.9$) and at forward rapidity ($2.5 < y < 4$). Figure 3 shows the J/ψ yields obtained at midrapidity for the 0–10% and 30–50% centrality intervals, while Fig. 4 shows the yields measured at forward rapidity in the 0–20%, 20–40% and 40–90% centrality intervals. For all of the results, the statistical and systematic uncertainties

are indicated by the vertical error bars and the open boxes around the data points, respectively. These results are compared with calculations performed using the statistical hadronisation model (SHMc) by Andronic et al. [32], and two microscopic transport models by Rapp et al. [70] and Zhuang et al. [33]. The physics assumptions in these model calculations are discussed in more detail in the next section. The lower panels of the Figs. 3 and 4 depict the ratio between the experimental data and the different model calculations, with the width of the bands representing the model uncertainties. These uncertainties are due to uncertainties on input parameters, mainly the total charm-quark production cross section and CNM effects. The filled boxes around unity represent the uncertainties of the measured results, shown as the quadratic sum of statistical and systematic uncertainties. Both transport models describe the p_T -differential yields in central and semicentral collisions, while they overestimate them at forward rapidity in peripheral collisions. The SHMc calculations coupled with a hydrodynamics inspired freeze-out parameterisation are in good agreement with the data in the low- p_T region, but underestimate the measurements at higher p_T .

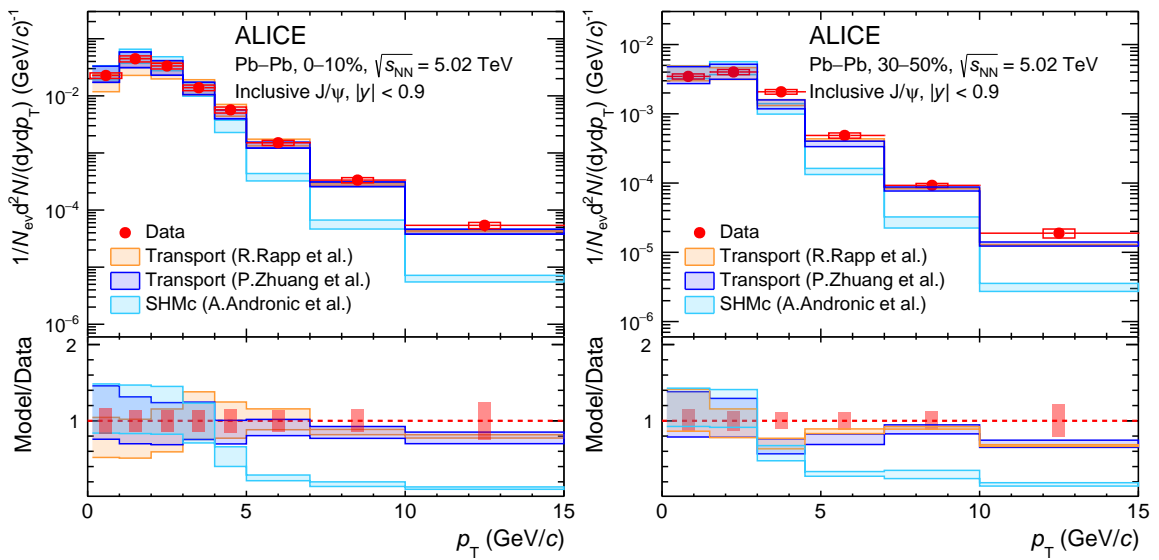


Figure 3: J/ψ p_T -differential production yields in Pb–Pb collisions at $\sqrt{s_{NN}} = 5.02$ TeV at midrapidity in the 0–10% (left panel) and 30–50% (right panel) centrality intervals. The statistical and systematic uncertainties are indicated, respectively, by the vertical error bars and the open boxes. The horizontal bars indicate the p_T intervals. Data are compared to model calculations from Refs. [32, 33, 70]. The ratios between data and models are shown in the lower panels. The filled boxes around unity depict the quadratic sum of statistical and systematic uncertainties from the measurement, while the bands indicate model uncertainties.

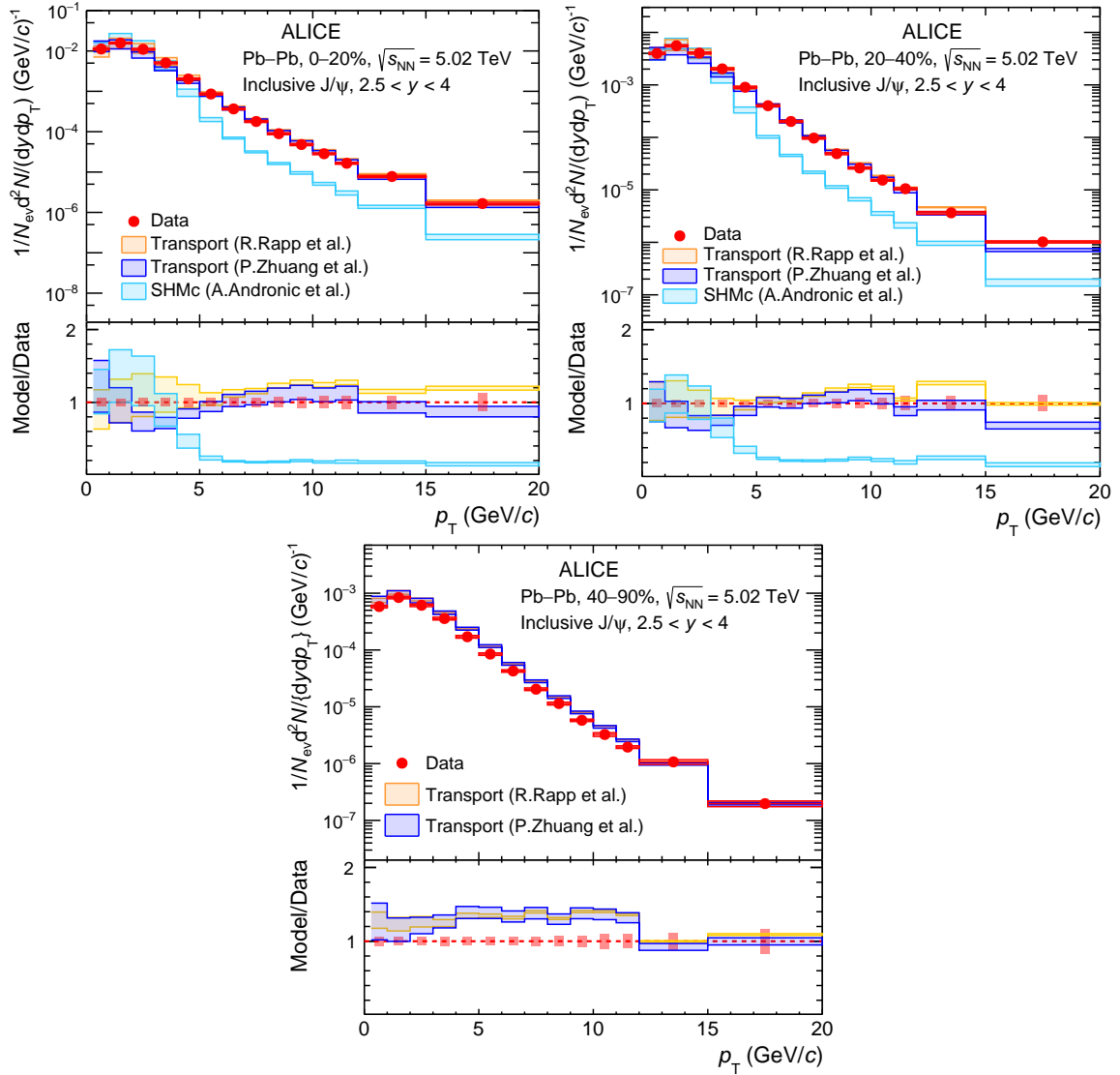


Figure 4: J/ψ p_T -differential production yields in Pb–Pb collisions at $\sqrt{s_{\text{NN}}} = 5.02$ TeV at forward rapidity in the 0–20%, 20–40%, and 40–90% centrality intervals. The statistical and systematic uncertainties are indicated, respectively, by the vertical error bars and the open boxes. The horizontal bars indicate the p_T intervals. Data are compared to model calculations from Refs. [32, 33, 70]. The ratio between data and models is shown in the lower panels. The filled boxes around unity depict the quadratic sum of statistical and systematic uncertainties from the measurement, while the bands indicate model uncertainties.

4.2 The J/ψ nuclear modification factor R_{AA}

The nuclear modification factor R_{AA} was obtained using the measured yields, according to Eq. 2. Figure 5 shows the p_T -integrated J/ψ R_{AA} as a function of N_{part} in Pb–Pb collisions at $\sqrt{s_{\text{NN}}} = 5.02$ TeV, obtained in the current analysis at midrapidity in comparison to the results at forward rapidity, previously reported by the ALICE Collaboration in Ref. [19]. Global uncertainties represented the centrality-correlated uncertainties, shown as filled boxes around unity, and are largely uncorrelated between the forward and midrapidity analyses. Both results exclude low- p_T J/ψ , with a selection of $p_T > 0.15$ GeV/ c and $p_T > 0.3$ GeV/ c at midrapidity and forward rapidity, respectively, in order to reject J/ψ produced via photoproduction processes [71–73], which contribute significantly to the J/ψ yield in particular in peripheral collisions [74, 75]. The R_{AA} is compatible with unity in the most peripheral collisions, while

a suppression of the J/ψ production in Pb–Pb collisions with respect to binary scaled pp collisions is observed in semicentral and central collisions, in particular at forward rapidity. At midrapidity, R_{AA} exhibits a slightly increasing trend from approximately $\langle N_{\text{part}} \rangle = 100$ towards the most central collisions, with slightly larger R_{AA} values at midrapidity than at forward rapidity, which confirms previous observations reported by ALICE [21]. The results at midrapidity are larger than those measured at forward rapidity, with a significance of the difference of 2.2σ when considering the data points in the centrality range 0–10%. The larger R_{AA} in central collisions at midrapidity is expected in phenomenological models due to the larger $d\sigma_{c\bar{c}}/dy$ at midrapidity which leads to larger fraction of J/ψ produced via (re)generation [32, 33, 76].

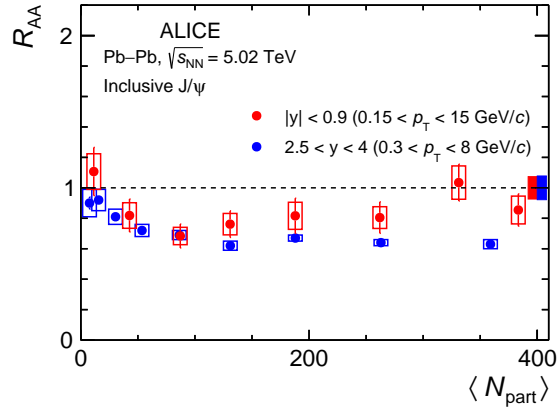


Figure 5: Inclusive J/ψ nuclear modification factor at midrapidity and forward rapidity [19], integrated over p_{T} , as a function of the number of participants in Pb–Pb collisions at $\sqrt{s_{\text{NN}}} = 5.02$ TeV. The statistical and systematic uncertainties are indicated, respectively, by the vertical error bars and the open boxes around the data points. The filled boxes around unity show the global uncertainties.

The p_{T} -differential R_{AA} results are shown in Fig. 6 for midrapidity (left panel) and forward rapidity (right panel) in various centrality intervals. The main feature of these measurements is that the R_{AA} values are relatively large at low p_{T} ($p_{\text{T}} < 5$ GeV/ c), in contrast with the strong suppression in the $p_{\text{T}} > 5$ GeV/ c range, for central and semicentral collisions. A weaker p_{T} dependence of the R_{AA} values is observed from central to peripheral collisions, up to a constant R_{AA} , within uncertainties, in the 40–90% centrality interval at forward rapidity. Such a behaviour in the data can be qualitatively understood by the dominance of hot nuclear matter effects for central and semicentral collisions, acting on top of the CNM ones, which were discussed in Refs. [39, 44]. In the low- p_{T} region and in particular in central and semicentral collisions, where the density of charm quarks is larger, the coalescence of charm quark pairs has an important contribution counterbalancing the impact of quarkonium suppression in the QGP. At higher p_{T} , the J/ψ production is dominated by effects such as dissociation and energy loss, which are expected to be stronger in the most central collisions. A comparison of the J/ψ p_{T} -differential R_{AA} in the most central Pb–Pb collisions at $\sqrt{s_{\text{NN}}} = 5.02$ TeV between midrapidity and forward rapidity is shown in Fig. 7. Neglecting the slight difference in centrality intervals, the R_{AA} is higher at midrapidity with respect to forward rapidity at low p_{T} ($p_{\text{T}} < 3$ GeV/ c) with a 2.7σ significance, highlighting the strong dependence of R_{AA} on the local charm quark density, further supporting the picture of quarkonium production via coalescing charm quarks. The two measurements converge to similar values at higher p_{T} suggesting a weaker dependence on rapidity for the suppression effects.

The measurements presented so far are discussed in the rest of this section in comparison to calculations which employ different approaches in modelling the collision fireball and the hot medium effects having an impact on J/ψ production in Pb–Pb collisions.

The statistical hadronisation model by Andronic et al. [32] assumes that all charm quarks are produced

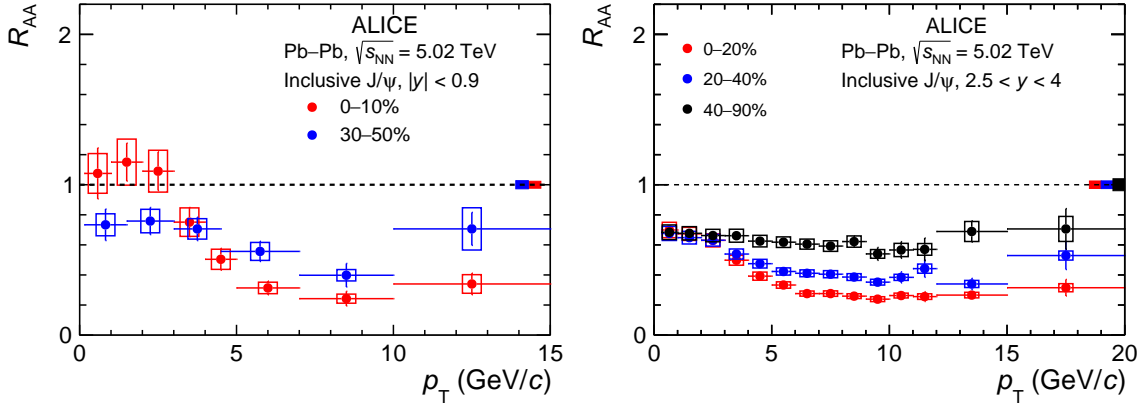


Figure 6: Inclusive J/ψ p_T -differential R_{AA} in Pb–Pb collisions at $\sqrt{s_{NN}} = 5.02$ TeV in various centrality intervals. The left panel shows the comparison of R_{AA} measured in central (0–10%) and semicentral (30–50%) collisions at midrapidity. The right panel shows the measured R_{AA} in three centrality classes, 0–20%, 20–40%, and 40–90%, at forward rapidity. The statistical and systematic uncertainties are indicated, respectively, by the vertical error bars and the open boxes around the data points. The filled boxes around unity show the global uncertainties.

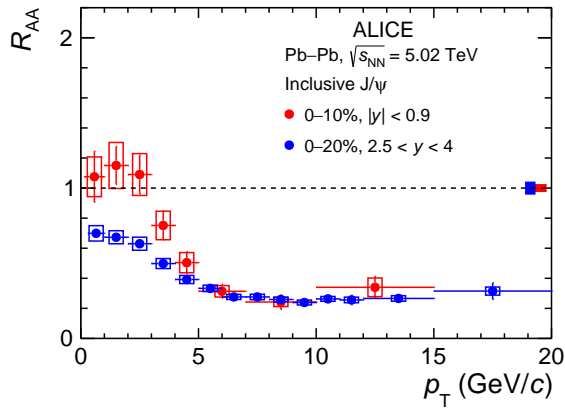


Figure 7: Inclusive J/ψ R_{AA} as a function of p_T in Pb–Pb collisions at $\sqrt{s_{NN}} = 5.02$ TeV at midrapidity and forward rapidity, in the 0–10% centrality class and 0–20% centrality class, respectively. The statistical and systematic uncertainties are indicated, respectively, by the vertical error bars and the open boxes around the data points. The filled boxes around unity show the global uncertainties.

during the initial hard partonic interactions and then thermalize in the QGP. The relative yields of the charmed hadrons are then determined solely by the equilibrium thermodynamical parameters at the chemical freeze-out, which are fixed from fits to the yields of light-flavoured hadrons. A recent extension of the model [30, 32] implements a hydro-inspired freeze-out hypersurface which allows the calculation of p_T -differential yields in addition to the integrated ones.

The microscopic transport model of Zhuang et al. [33, 77] implements a real time evolution of the J/ψ , $\psi(2S)$ and χ_c production using a Boltzmann-type rate equation that includes both dissociation and coalescence terms. The dissociation term includes contributions from the temperature dependent colour screening effect and scatterings with thermal partons, i.e. gluon dissociation. The (re)generation of charmonia is implemented by exploiting the detailed balance of the gluon dissociation process. The space–time evolution of the fireball is described using the equations for (2+1)D ideal hydrodynamics. This model includes also the production of non-prompt J/ψ , with the precursor beauty quarks being propagated through the QGP using the Langevin equation.

Similarly to the previously described model, the transport model proposed by Rapp et al. [76, 78–81], is also based on a kinetic rate equation to compute the time evolution of charmonium (J/ψ , $\psi(2S)$, and χ_c) yields. The dissociation term of the rate equation employs an inelastic parton scattering cross section of charmonia in the QGP, computed using next-to-leading order perturbative QCD Feynman diagrams, and also includes the effect of in-medium reduced binding energy. The (re)generation rate depends on the charmonium dissociation temperature, which is extracted from lattice QCD calculations, and equilibrium limits computed based on the thermal model. The space–time evolution of heavy-ion collisions is simulated by a cylindrically expanding fireball model with the regenerated charmonium p_T -spectra being calculated in a thermal blast-wave approximation at a temperature and flow velocity reflecting the average production time of each charmonium state [82].

All of the models described above consider the initial state of the nuclear collisions by making assumptions on the total charm quark density produced during the hard partonic collisions and modified by the CNM effects. The two transport models obtain the total charm density based on the measured total charm cross section in pp collisions [83] multiplied by the number of binary nucleon–nucleon collisions. The CNM effects are introduced via different approaches. The microscopic transport model of Rapp et al. [78, 79] estimates CNM effects using fits of the measured p–A data, while the transport model of Zhuang et al. [80, 81] uses the EPS09 model [84], which provides the nuclear parton distribution functions and their uncertainties from different types of experimental inputs. The SHMc extracts the total charm cross section from the ALICE measurements of D meson production in Pb–Pb collisions [85]. The large uncertainty on the estimation of CNM effects is inherited by these model calculations.

At large p_T , the fragmentation of high-energy partons may become the main mechanism for J/ψ production. In that case, energy loss of partons due to multiple scattering in the QGP leads to J/ψ suppression at high p_T . In the model by Arleo et al. [35], the quenching of large- p_T particles ($p_T > 10$ GeV/ c) is assumed to be mostly due to radiative parton energy loss. In this approach, the p_T dependence of R_{AA} is fully predicted from the model proposed by Baier et al. [86, 87], which employed a medium-induced gluon spectrum. The R_{AA} value is computed from the mean energy loss, which is extracted from a fit to the charged hadron R_{AA} , measured in various collision systems, the average fragmentation function, and the colour coupling factor of the parton. At forward rapidity, the mean energy loss is further corrected for the charged-hadron multiplicity difference between midrapidity and forward rapidity. The model uncertainties arise from the uncertainties on these inputs. This model does not include the production of non-prompt J/ψ , but the R_{AA} variation, when accounting for this contribution, is expected to lie within the theoretical uncertainties.

The p_T -integrated nuclear modification factor measured in Pb–Pb collisions at $\sqrt{s_{\text{NN}}} = 5.02$ TeV at midrapidity is shown in Fig. 8 in comparison with results from the SHMc and the two transport-model calculations. The calculations are shown as coloured bands, illustrating the uncertainties on the initial effects, mainly CNM effects, described above. Within the model uncertainties, all three predictions agree with the data. One can note though that the data lie on the upper edge of the transport-model calculations, while they are in good agreement with the central values from the SHMc calculations for semicentral and central collisions.

Figures 9 and 10 show the p_T -differential R_{AA} measurements for various centrality intervals at midrapidity and forward rapidity, respectively, in comparison with the available model calculations. With the exception of the energy-loss calculations, available only for $p_T > 10$ GeV/ c , all of the models cover the full p_T range in which these measurements were performed. The SHMc model calculations are in good agreement with the data at low p_T at both midrapidity and forward rapidity. However, the R_{AA} is underestimated for $p_T > 5$ GeV/ c in all centrality intervals in both rapidity ranges. This might be attributed to physical sources missing in this approach, such as the contributions from surviving primordial J/ψ or non-prompt J/ψ from beauty-hadron decays, but also to an underestimated amount of radial flow acquired by the charm quarks during the system evolution. A similar conclusion can also be drawn from

the comparison of the p_T -differential yields in Pb–Pb collisions shown in Fig. 3 where the measured spectrum is harder than the one from the SHMc calculations. The two transport models are in better quantitative agreement with data than the SHMc model. Both of the transport models provide a good description of the R_{AA} at both low and high p_T . However, the model calculations in the low- p_T region, where J/ψ production is dominated by coalescence in these models, do not describe the detailed shape of the p_T dependence of R_{AA} , in particular in semicentral collisions, which points to a still not perfectly understood dynamics of charm-quark coalescence.

The energy-loss calculations by Arleo et al [35], performed in all studied centrality ranges for $p_T > 10$ GeV/c, are in good agreement with the measurements, which, based on the model assumptions, suggests that the dominant mechanism in this kinematic regime is indeed energy loss, similar to that of the other hadrons measured at LHC energies.

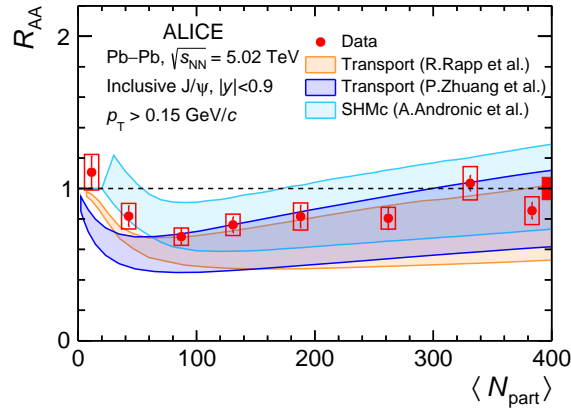


Figure 8: Inclusive J/ψ R_{AA} at midrapidity, integrated over p_T , as a function of N_{part} in Pb–Pb collisions at $\sqrt{s_{NN}} = 5.02$ TeV and compared to model calculations from Refs. [32, 33, 70].

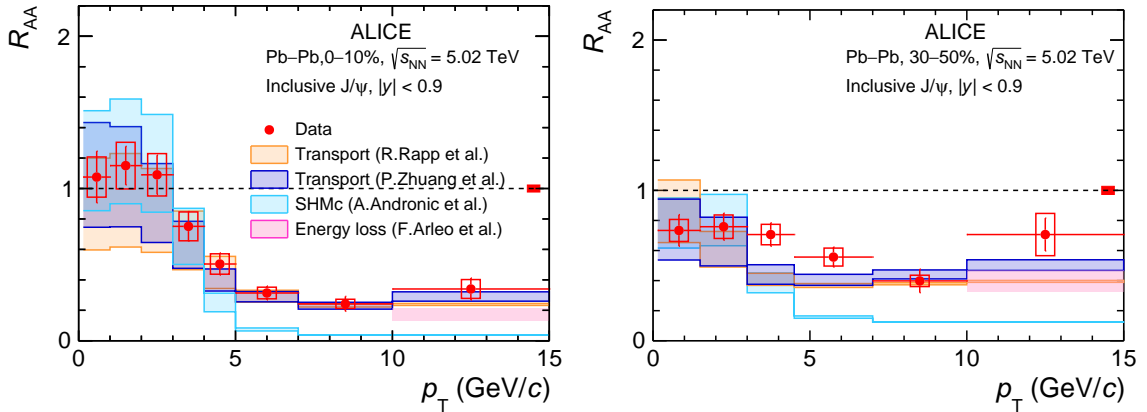


Figure 9: Transverse-momentum dependence of the J/ψ R_{AA} in Pb–Pb collisions at $\sqrt{s_{NN}} = 5.02$ TeV at midrapidity in the 0–10% (left panel) and 30–50% (right panel) centrality intervals. The data are compared with model calculations from Refs. [32, 33, 35, 70].

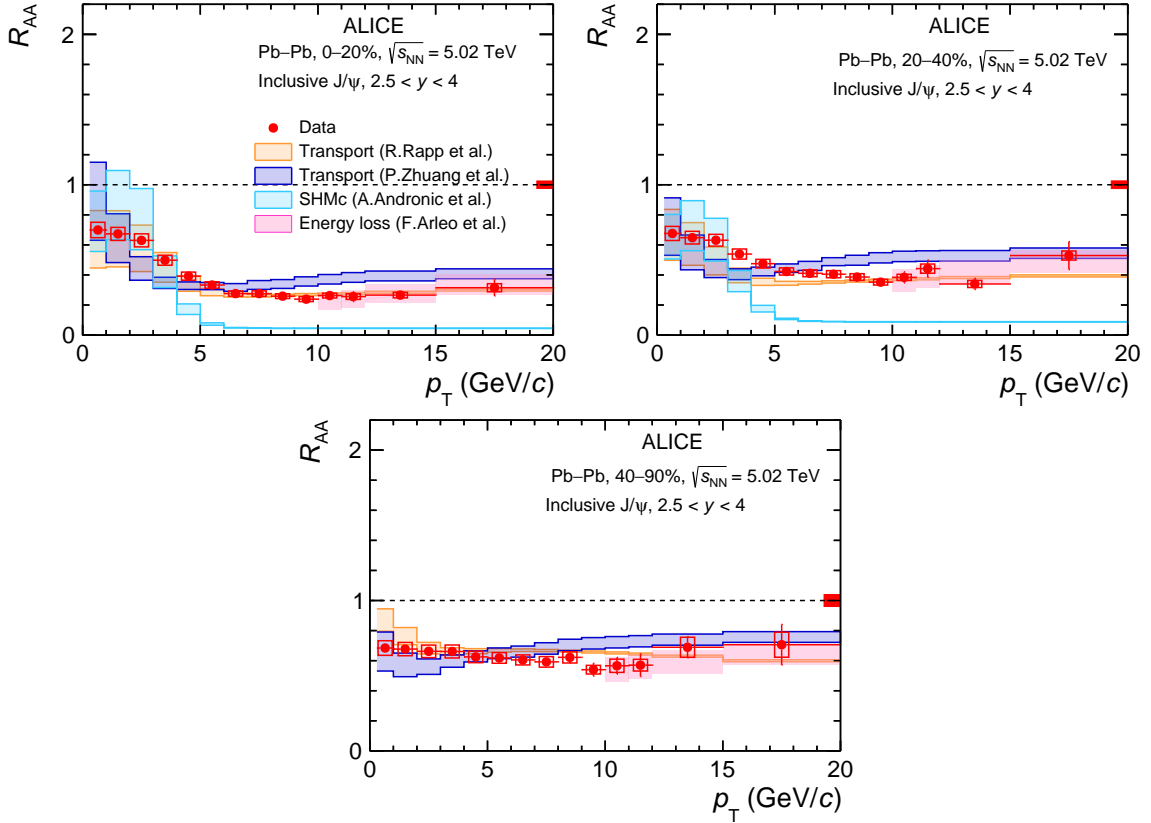


Figure 10: Transverse-momentum dependence of the J/ψ R_{AA} at forward rapidity in the 0–20%, 20–40% and 40–90% centrality intervals. The data are compared with model calculations from Refs. [32, 33, 35, 70]

4.3 The inclusive J/ψ $\langle p_T \rangle$ and $\langle p_T^2 \rangle$

Observables that allow for a more differential study of the J/ψ p_T spectrum with respect to the centrality of the collisions are the J/ψ $\langle p_T \rangle$ and $\langle p_T^2 \rangle$. The latter is typically quantified using the r_{AA} , defined in Eq.3, which is related to the broadening or narrowing of the J/ψ p_T spectrum relative to that in pp collisions. The $\langle p_T \rangle$ and the r_{AA} measured at midrapidity are shown in Fig. 11 in the left and right panels, respectively, as a function of $\langle N_{part} \rangle$. Similar measurements were done at the forward rapidity as well [20]. These results are compared with similar measurements in heavy-ion collisions at RHIC [11, 26, 88] and SPS [89] energies. The $\langle p_T \rangle$ results are also compared with the value reported by the ALICE Collaboration in pp collisions at midrapidity at $\sqrt{s} = 5.02$ TeV [69], showing a good agreement with the value measured in the most peripheral Pb–Pb collisions. The data show that for a given N_{part} , the J/ψ $\langle p_T \rangle$ grows with increasing collision energy. However, while the data indicate no centrality dependence of the $\langle p_T \rangle$ at the SPS and RHIC energies, a monotonically decreasing trend from the most peripheral to the most central collisions is observed in the ALICE measurements, which reflects the gradual increase of the low p_T (re)generation component. The r_{AA} results support the observations for the $\langle p_T \rangle$, showing a decrease from unity towards central collisions for the ALICE measurements. The RHIC results are compatible with unity over the whole covered centrality range, while the SPS data indicate a strong increase from peripheral to central collisions, suggesting that CNM effects such as the Cronin effect [90] have an impact on the J/ψ p_T shape.

The $\langle p_T \rangle$ and $\langle p_T^2 \rangle$ results are also compared with the aforementioned transport model calculations, which show a good agreement with the trends observed in data as demonstrated in Fig. 12. Although overall in good quantitative agreement, the calculations by Rapp et al. overestimate the J/ψ $\langle p_T \rangle$ for the most central collisions, while the $\langle p_T^2 \rangle$ results are slightly underestimated by both models in the semicentral

and peripheral range ($50 < N_{\text{part}} < 150$).

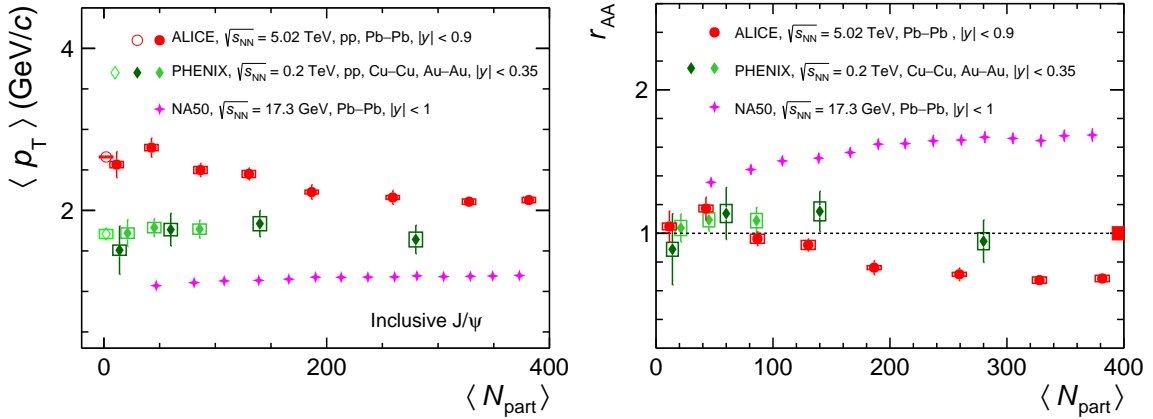


Figure 11: Left panel: Inclusive J/ψ $\langle p_T \rangle$ as a function of the mean number of participants in Pb–Pb collisions at $\sqrt{s_{NN}} = 5.02$ TeV at midrapidity. Right panel: Inclusive J/ψ r_{AA} as a function of centrality at $\sqrt{s_{NN}} = 5.02$ TeV and compared with measurements at lower energies from RHIC [11, 88, 91] and the SPS [89]. The statistical and systematic uncertainties are indicated, respectively, by the vertical error bars and the open boxes around the data points. The filled box around unity on the right panel shows the global uncertainty.

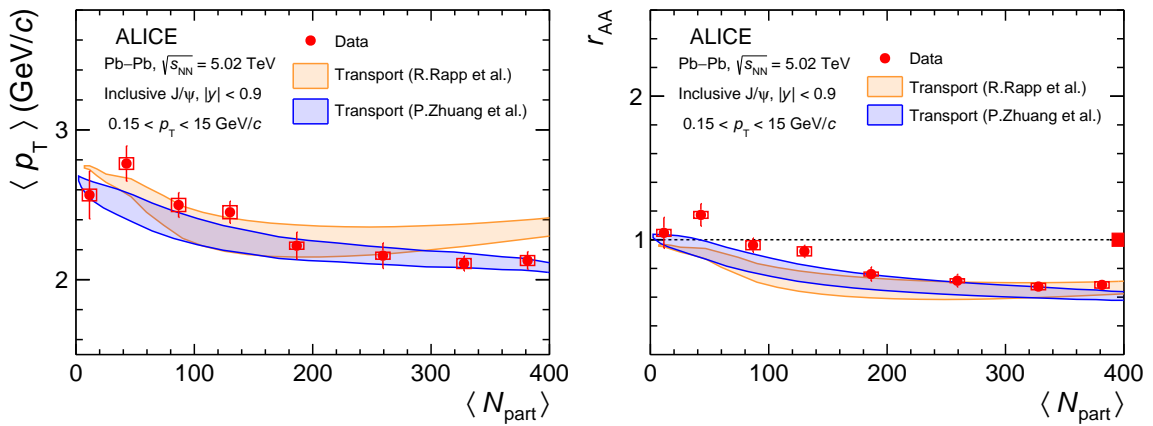


Figure 12: Inclusive J/ψ $\langle p_T \rangle$ as a function of the mean number of participants in Pb–Pb collisions at $\sqrt{s_{NN}} = 5.02$ TeV at midrapidity (left panel), and J/ψ r_{AA} as a function of centrality (right panel). The results are compared with transport model calculations [33, 70]

4.4 The J/ψ to D^0 yield ratio

A long awaited measurement which helps understanding the details of the J/ψ production in heavy-ion collisions is the ratio between the J/ψ and the D^0 yields, both measured in the same collision system. Such a measurement provides a tight constraint to models because some of the model parameters and most model uncertainties related to the $c\bar{c}$ cross section cancel in the ratio. This ratio is sensitive to the hadronisation mechanisms of the different charm hadrons. While a model independent measurement of the $c\bar{c}$ production density in heavy-ion collisions is not available, it is still useful to compare the J/ψ yield with the recently published ALICE measurements of the D^0 yield down to zero p_T [85].

Figure 13 shows the measured p_T -integrated J/ψ to D^0 yield ratio in central (0–10%) and semicentral (30–50%) collisions. The largest source of systematic uncertainty for both measurements comes from tracking efficiency and it is considered correlated between the D^0 and J/ψ measurements, and

consequently cancels in the ratio. Without this uncertainty, the numerical values of the J/ψ yields are 0.12 ± 0.005 (stat.) ± 0.012 (syst.) and 0.016 ± 0.0008 (stat.) ± 0.0004 (syst.) for (0–10%) and (30–50%) centrality intervals, respectively. The statistical (systematical) uncertainty of the ratio is the quadratic sum of the statistical (systematical) uncertainties of the two measurements. The results suggest a higher value for this ratio in central compared to semicentral collisions. This is supported by the SHMc calculations [32], which suggests both the J/ψ and D^0 are produced via the coalescence of charm quarks at the phase boundary, the ratio being determined by the charm fugacity. The SHMc model give a good description of the data. The model uncertainty from the SHMc model is due to uncertainties on the charm fugacity parameter, which is fitted to the ALICE D^0 data [85].

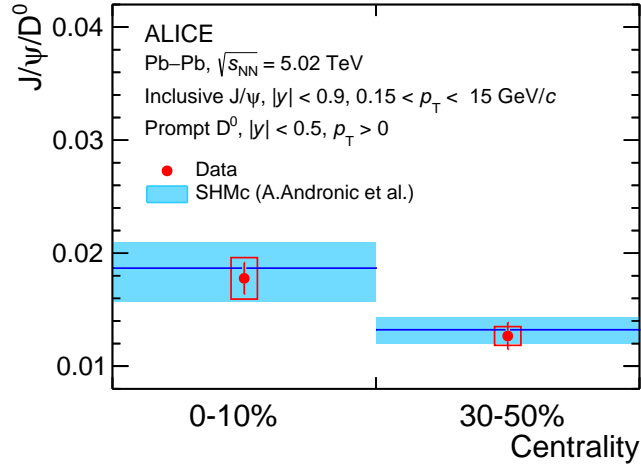


Figure 13: Inclusive J/ψ to D^0 yield [85] ratio at $\sqrt{s_{NN}} = 5.02$ TeV at midrapidity for the 0–10% and 30–50% centrality intervals. Vertical lines and open boxes represent the statistical and systematical uncertainties, respectively. The measurements are compared with SHMc model predictions [32].

5 Conclusions

The J/ψ p_T -differential yields and nuclear modification factors R_{AA} measured from $p_T = 0.15$ GeV/c up to 15 GeV/c in the 0–10% and 30–50% centrality ranges at midrapidity and from $p_T = 0.3$ GeV/c up to $p_T = 20$ GeV/c in the 0–20%, 20–40% and 40–90% centrality ranges at forward rapidity, and the centrality dependent J/ψ $\langle p_T \rangle$ and r_{AA} measured at midrapidity, are reported and discussed in comparison with model calculations.

The centrality dependent p_T -integrated R_{AA} in peripheral collisions shows similar values at both midrapidity and forward rapidity, while a hint of an increasing trend of the R_{AA} is observed at midrapidity towards central collisions. When looking at the p_T -differential R_{AA} , relatively large values are observed at low p_T , which are compatible with unity for $p_T < 3$ GeV/c in the 0–10% centrality interval at $|y| < 0.9$, while a strong nuclear suppression is seen at higher p_T in central and semicentral collisions. In addition, R_{AA} is higher at midrapidity than at forward rapidity for $p_T < 3$ GeV/c in the most central collisions. A weaker p_T dependence of the R_{AA} values is observed for more peripheral collisions. Such a behaviour, for the central and semicentral collisions, can be explained by a large contribution from (re)generation to the J/ψ yields. This is supported by the statistical hadronisation model and by two microscopic transport model calculations when compared to the data. However, the large model uncertainties, which are mainly due to the assumptions on the collision initial conditions, prevent from drawing a clear conclusion on the phenomenology of the J/ψ production in heavy-ion collisions at LHC energies. The J/ψ nuclear modification factor at high p_T is well described by the transport models and also by a J/ψ energy loss model, while it is largely underestimated in the hydro-inspired freeze-out approach implemented together with

the SHMc model. For most central events, the R_{AA} converge to similar values at high p_T at mid and forward rapidity suggesting a weaker dependence on rapidity for the suppression effects. The centrality dependent $J/\psi \langle p_T \rangle$ and r_{AA} measurements are compared with similar results at lower energies from RHIC [11, 88, 91] and SPS [89], with the centrality trends showing an opposite behaviour between the LHC and the lower energy results. This behaviour is compatible with a strong contribution from the regeneration component which tends to soften the p_T distributions. The two microscopic transport models describe the data within the uncertainties.

The ratio of inclusive p_T -integrated J/ψ to D^0 yields measured by ALICE at midrapidity in Pb–Pb collisions is shown for the first time in the 0–10% and 30–50% centrality ranges. The data shows a larger value of this ratio in 0–10% compared to 30–50% collisions which, is in good agreement with the expectation from the SHMc model that fixes the charm fugacity parameter based on the D^0 yields measured by ALICE.

The large improvements in experimental accuracy expected for the LHC Run 3 and 4 for charmonium measurements and more in general for heavy-quark production, will allow to settle the longstanding questions regarding the mechanisms behind charmonium production in heavy-ion collisions.

Acknowledgements

We would like to thank the theory groups who kindly provided us with their calculations and for the fruitful discussions.

The ALICE Collaboration would like to thank all its engineers and technicians for their invaluable contributions to the construction of the experiment and the CERN accelerator teams for the outstanding performance of the LHC complex. The ALICE Collaboration gratefully acknowledges the resources and support provided by all Grid centres and the Worldwide LHC Computing Grid (WLCG) collaboration. The ALICE Collaboration acknowledges the following funding agencies for their support in building and running the ALICE detector: A. I. Alikhanyan National Science Laboratory (Yerevan Physics Institute) Foundation (ANSL), State Committee of Science and World Federation of Scientists (WFS), Armenia; Austrian Academy of Sciences, Austrian Science Fund (FWF): [M 2467-N36] and Nationalstiftung für Forschung, Technologie und Entwicklung, Austria; Ministry of Communications and High Technologies, National Nuclear Research Center, Azerbaijan; Conselho Nacional de Desenvolvimento Científico e Tecnológico (CNPq), Financiadora de Estudos e Projetos (Finep), Fundação de Amparo à Pesquisa do Estado de São Paulo (FAPESP) and Universidade Federal do Rio Grande do Sul (UFRGS), Brazil; Bulgarian Ministry of Education and Science, within the National Roadmap for Research Infrastructures 2020;2027 (object CERN), Bulgaria; Ministry of Education of China (MOEC), Ministry of Science & Technology of China (MSTC) and National Natural Science Foundation of China (NSFC), China; Ministry of Science and Education and Croatian Science Foundation, Croatia; Centro de Aplicaciones Tecnológicas y Desarrollo Nuclear (CEADEN), Cubaenergía, Cuba; Ministry of Education, Youth and Sports of the Czech Republic, Czech Republic; The Danish Council for Independent Research | Natural Sciences, the VILLUM FONDEN and Danish National Research Foundation (DNRF), Denmark; Helsinki Institute of Physics (HIP), Finland; Commissariat à l’Energie Atomique (CEA) and Institut National de Physique Nucléaire et de Physique des Particules (IN2P3) and Centre National de la Recherche Scientifique (CNRS), France; Bundesministerium für Bildung und Forschung (BMBF) and GSI Helmholtzzentrum für Schwerionenforschung GmbH, Germany; General Secretariat for Research and Technology, Ministry of Education, Research and Religions, Greece; National Research, Development and Innovation Office, Hungary; Department of Atomic Energy Government of India (DAE), Department of Science and Technology, Government of India (DST), University Grants Commission, Government of India (UGC) and Council of Scientific and Industrial Research (CSIR), India; National Research and Innovation Agency - BRIN, Indonesia; Istituto Nazionale di Fisica Nucleare (INFN), Italy;

Japanese Ministry of Education, Culture, Sports, Science and Technology (MEXT) and Japan Society for the Promotion of Science (JSPS) KAKENHI, Japan; Consejo Nacional de Ciencia (CONACYT) y Tecnología, through Fondo de Cooperación Internacional en Ciencia y Tecnología (FONCICYT) and Dirección General de Asuntos del Personal Académico (DGAPA), Mexico; Nederlandse Organisatie voor Wetenschappelijk Onderzoek (NWO), Netherlands; The Research Council of Norway, Norway; Commission on Science and Technology for Sustainable Development in the South (COMSATS), Pakistan; Pontificia Universidad Católica del Perú, Peru; Ministry of Education and Science, National Science Centre and WUT ID-UB, Poland; Korea Institute of Science and Technology Information and National Research Foundation of Korea (NRF), Republic of Korea; Ministry of Education and Scientific Research, Institute of Atomic Physics, Ministry of Research and Innovation and Institute of Atomic Physics and University Politehnica of Bucharest, Romania; Ministry of Education, Science, Research and Sport of the Slovak Republic, Slovakia; National Research Foundation of South Africa, South Africa; Swedish Research Council (VR) and Knut & Alice Wallenberg Foundation (KAW), Sweden; European Organization for Nuclear Research, Switzerland; Suranaree University of Technology (SUT), National Science and Technology Development Agency (NSTDA), Thailand Science Research and Innovation (TSRI) and National Science, Research and Innovation Fund (NSRF), Thailand; Turkish Energy, Nuclear and Mineral Research Agency (TENMAK), Turkey; National Academy of Sciences of Ukraine, Ukraine; Science and Technology Facilities Council (STFC), United Kingdom; National Science Foundation of the United States of America (NSF) and United States Department of Energy, Office of Nuclear Physics (DOE NP), United States of America. In addition, individual groups or members have received support from: European Research Council, Strong 2020 - Horizon 2020 (grant nos. 950692, 824093), European Union; Academy of Finland (Center of Excellence in Quark Matter) (grant nos. 346327, 346328), Finland; Programa de Apoyos para la Superación del Personal Académico, UNAM, Mexico.

References

- [1] A. Bazavov *et al.*, “Equation of state and QCD transition at finite temperature”, *Phys. Rev. D* **80** (2009) 014504, arXiv:0903.4379 [hep-lat].
- [2] S. Borsanyi, Z. Fodor, C. Hoelbling, S. D. Katz, S. Krieg, and K. K. Szabo, “Full result for the QCD equation of state with 2+1 flavors”, *Phys. Lett. B* **730** (2014) 99–104, arXiv:1309.5258 [hep-lat].
- [3] F. Prino and R. Rapp, “Open heavy flavor in QCD matter and in nuclear collisions”, *J. Phys. G* **43** (2016) 093002, arXiv:1603.00529 [nucl-ex].
- [4] A. Rothkopf, “Heavy Quarkonium in Extreme Conditions”, *Phys. Rept.* **858** (2020) 1–117, arXiv:1912.02253 [hep-ph].
- [5] N. Brambilla *et al.*, “Heavy Quarkonium: Progress, Puzzles, and Opportunities”, *Eur. Phys. J. C* **71** (2011) 1534, arXiv:1010.5827 [hep-ph].
- [6] T. Matsui and H. Satz, “ J/ψ Suppression by Quark-Gluon Plasma Formation”, *Phys. Lett.* **B178** (1986) 416–422.
- [7] S. Digal, P. Petreczky, and H. Satz, “Quarkonium feed down and sequential suppression”, *Phys. Rev. D* **64** (2001) 094015, arXiv:hep-ph/0106017.
- [8] NA38 Collaboration, C. Baglin *et al.*, “ ψ' and J/ψ production in pW, pU and SU interactions at 200-GeV/nucleon”, *Phys. Lett. B* **345** (1995) 617–621.
- [9] NA50 Collaboration, B. Alessandro *et al.*, “A new measurement of J/ψ suppression in Pb–Pb collisions at 158-GeV per nucleon”, *Eur. Phys. J. C* **39** (2005) 335–345, arXiv:hep-ex/0412036.

- [10] **NA60** Collaboration, R. Arnaldi *et al.*, “ J/ψ production in indium-indium collisions at 158-GeV/nucleon”, *Phys. Rev. Lett.* **99** (2007) 132302.
- [11] **PHENIX** Collaboration, A. Adare *et al.*, “ J/ψ Production vs Centrality, Transverse Momentum, and Rapidity in Au+Au Collisions at $\sqrt{s_{NN}} = 200$ GeV”, *Phys. Rev. Lett.* **98** (2007) 232301, arXiv:nucl-ex/0611020.
- [12] **PHENIX** Collaboration, A. Adare *et al.*, “ J/ψ suppression at forward rapidity in Au+Au collisions at $\sqrt{s_{NN}} = 200$ GeV”, *Phys. Rev. C* **84** (2011) 054912, arXiv:1103.6269 [nucl-ex].
- [13] **STAR** Collaboration, B. I. Abelev *et al.*, “ J/ψ production at high transverse momentum in p+p and Cu+Cu collisions at $\sqrt{s_{NN}} = 200$ GeV”, *Phys. Rev. C* **80** (2009) 041902, arXiv:0904.0439 [nucl-ex].
- [14] **STAR** Collaboration, L. Adamczyk *et al.*, “ J/ψ production at low p_T in Au + Au and Cu + Cu collisions at $\sqrt{s_{NN}} = 200$ GeV with the STAR detector”, *Phys. Rev. C* **90** (2014) 024906, arXiv:1310.3563 [nucl-ex].
- [15] **CMS** Collaboration, S. Chatrchyan *et al.*, “Suppression of non-prompt J/ψ , prompt J/ψ , and $Y(1S)$ in PbPb collisions at $\sqrt{s_{NN}} = 2.76$ TeV”, *JHEP* **05** (2012) 063, arXiv:1201.5069 [nucl-ex].
- [16] **ALICE** Collaboration, B. Abelev *et al.*, “ J/ψ suppression at forward rapidity in Pb–Pb collisions at $\sqrt{s_{NN}} = 2.76$ TeV”, *Phys. Rev. Lett.* **109** (2012) 072301, arXiv:1202.1383 [hep-ex].
- [17] **ALICE** Collaboration, B. Abelev *et al.*, “Centrality, rapidity and transverse momentum dependence of J/ψ suppression in Pb–Pb collisions at $\sqrt{s_{NN}}=2.76$ TeV”, *Phys. Lett. B* **734** (2014) 314–327, arXiv:1311.0214 [nucl-ex].
- [18] **ALICE** Collaboration, J. Adam *et al.*, “Differential studies of inclusive J/ψ and $\psi(2S)$ production at forward rapidity in Pb–Pb collisions at $\sqrt{s_{NN}} = 2.76$ TeV”, *JHEP* **05** (2016) 179, arXiv:1506.08804 [nucl-ex].
- [19] **ALICE** Collaboration, J. Adam *et al.*, “ J/ψ suppression at forward rapidity in Pb–Pb collisions at $\sqrt{s_{NN}} = 5.02$ TeV”, *Phys. Lett. B* **766** (2017) 212–224, arXiv:1606.08197 [nucl-ex].
- [20] **ALICE** Collaboration, S. Acharya *et al.*, “Studies of J/ψ production at forward rapidity in Pb–Pb collisions at $\sqrt{s_{NN}} = 5.02$ TeV”, *JHEP* **02** (2020) 041, arXiv:1909.03158 [nucl-ex].
- [21] **ALICE** Collaboration, S. Acharya *et al.*, “Centrality and transverse momentum dependence of inclusive J/ψ production at midrapidity in Pb–Pb collisions at $\sqrt{s_{NN}} = 5.02$ TeV”, *Phys. Lett. B* **805** (2020) 135434, arXiv:1910.14404 [nucl-ex].
- [22] **ALICE** Collaboration, “The ALICE experiment – A journey through QCD”, arXiv:2211.04384 [nucl-ex].
- [23] **ATLAS** Collaboration, M. Aaboud *et al.*, “Prompt and non-prompt J/ψ and $\psi(2S)$ suppression at high transverse momentum in 5.02 TeV Pb+Pb collisions with the ATLAS experiment”, *Eur. Phys. J. C* **78** (2018) 762, arXiv:1805.04077 [nucl-ex].
- [24] **CMS** Collaboration, A. M. Sirunyan *et al.*, “Measurement of prompt and nonprompt charmonium suppression in PbPb collisions at 5.02 TeV”, *Eur. Phys. J. C* **78** (2018) 509, arXiv:1712.08959 [nucl-ex].
- [25] **STAR** Collaboration, L. Adamczyk *et al.*, “Energy dependence of J/ψ production in Au+Au collisions at $\sqrt{s_{NN}} = 39, 62.4$ and 200 GeV”, *Phys. Lett. B* **771** (2017) 13–20.

- [26] **PHENIX** Collaboration, A. Adare *et al.*, “ J/ψ production in $\sqrt{s_{NN}} = 200$ GeV Cu–Cu collisions”, *Phys. Rev. Lett.* **101** (Sep, 2008) 122301.
- [27] **PHENIX** Collaboration, A. Adare *et al.*, “Forward J/ψ production in U+U collisions at $\sqrt{s_{NN}} = 193$ GeV”, *Phys. Rev. C* **93** (Mar, 2016) 034903.
- [28] **ALICE** Collaboration, S. Acharya *et al.*, “ J/ψ elliptic flow in Pb-Pb collisions at $\sqrt{s_{NN}} = 5.02$ TeV”, *Phys. Rev. Lett.* **119** (2017) 242301, arXiv:1709.05260 [nucl-ex].
- [29] **ALICE** Collaboration, S. Acharya *et al.*, “ J/ψ elliptic and triangular flow in Pb-Pb collisions at $\sqrt{s_{NN}} = 5.02$ TeV”, *JHEP* **10** (2020) 141, arXiv:2005.14518 [nucl-ex].
- [30] P. Braun-Munzinger and J. Stachel, “(Non)thermal aspects of charmonium production and a new look at J/ψ suppression”, *Phys. Lett. B* **490** (2000) 196–202, arXiv:nucl-th/0007059.
- [31] R. L. Thews, M. Schroedter, and J. Rafelski, “Enhanced J/ψ production in deconfined quark matter”, *Phys. Rev. C* **63** (2001) 054905, arXiv:hep-ph/0007323.
- [32] A. Andronic, P. Braun-Munzinger, M. K. Koehler, K. Redlich, and J. Stachel, “Transverse momentum distributions of charmonium states with the statistical hadronization model”, *Phys. Lett. B* **797** (2019) 134836, arXiv:1901.09200 [nucl-th].
- [33] K. Zhou, N. Xu, Z. Xu, and P. Zhuang, “Medium effects on charmonium production at ultrarelativistic energies available at the CERN Large Hadron Collider”, *Phys. Rev. C* **89** (2014) 054911, arXiv:1401.5845 [nucl-th].
- [34] X. Du and R. Rapp, “Sequential Regeneration of Charmonia in Heavy-Ion Collisions”, *Nucl. Phys. A* **943** (2015) 147–158, arXiv:1504.00670 [hep-ph].
- [35] F. Arleo, “Quenching of Hadron Spectra in Heavy Ion Collisions at the LHC”, *Phys. Rev. Lett.* **119** (2017) 062302, arXiv:1703.10852 [hep-ph].
- [36] E. G. Ferreira, “Charmonium dissociation and recombination at LHC: Revisiting comovers”, *Phys. Lett. B* **731** (2014) 57–63, arXiv:1210.3209 [hep-ph].
- [37] N. Armesto, “Nuclear shadowing”, *J. Phys. G* **32** (2006) R367–R394, arXiv:hep-ph/0604108.
- [38] **ALICE** Collaboration, B. Abelev *et al.*, “ J/ψ production and nuclear effects in p–Pb collisions at $\sqrt{s_{NN}} = 5.02$ TeV”, *JHEP* **02** (2014) 073, arXiv:1308.6726 [nucl-ex].
- [39] **ALICE** Collaboration, J. Adam *et al.*, “Rapidity and transverse-momentum dependence of the inclusive J/ψ nuclear modification factor in p–Pb collisions at $\sqrt{s_{NN}} = 5.02$ TeV”, *JHEP* **06** (2015) 055, arXiv:1503.07179 [nucl-ex].
- [40] **ALICE** Collaboration, J. Adam *et al.*, “Centrality dependence of inclusive J/ψ production in p–Pb collisions at $\sqrt{s_{NN}} = 5.02$ TeV”, *JHEP* **11** (2015) 127, arXiv:1506.08808 [nucl-ex].
- [41] **ALICE** Collaboration, S. Acharya *et al.*, “Inclusive J/ψ production at forward and backward rapidity in p–Pb collisions at $\sqrt{s_{NN}} = 8.16$ TeV”, *JHEP* **07** (2018) 160, arXiv:1805.04381 [nucl-ex].
- [42] **ALICE** Collaboration, S. Acharya *et al.*, “Prompt and non-prompt J/ψ production and nuclear modification at mid-rapidity in p–Pb collisions at $\sqrt{s_{NN}} = 5.02$ TeV”, *Eur. Phys. J. C* **78** (2018) 466, arXiv:1802.00765 [nucl-ex].

- [43] ALICE Collaboration, S. Acharya *et al.*, “Centrality dependence of J/ψ and $\psi(2S)$ production and nuclear modification in p-Pb collisions at $\sqrt{s_{NN}} = 8.16$ TeV”, *JHEP* **02** (2021) 002, arXiv:2008.04806 [nucl-ex].
- [44] ALICE Collaboration, S. Acharya *et al.*, “Inclusive, prompt and non-prompt J/ψ production at midrapidity in p-Pb collisions at $\sqrt{s_{NN}} = 5.02$ TeV”, *JHEP* **06** (2022) 011, arXiv:2105.04957 [nucl-ex].
- [45] ALICE Collaboration, K. Aamodt *et al.*, “The ALICE experiment at the CERN LHC”, *JINST* **3** (2008) S08002.
- [46] ALICE Collaboration, B. Abelev *et al.*, “Performance of the ALICE Experiment at the CERN LHC”, *Int. J. Mod. Phys. A* **29** (2014) 1430044, arXiv:1402.4476 [nucl-ex].
- [47] ALICE Collaboration, J. Alme *et al.*, “The ALICE TPC, a large 3-dimensional tracking device with fast readout for ultra-high multiplicity events”, *Nucl. Instrum. Meth. A* **622** (2010) 316–367, arXiv:1001.1950 [physics.ins-det].
- [48] ALICE Collaboration, K. Aamodt *et al.*, “Alignment of the ALICE Inner Tracking System with cosmic-ray tracks”, *JINST* **5** (2010) P03003, arXiv:1001.0502 [physics.ins-det].
- [49] ALICE Collaboration, *ALICE dimuon forward spectrometer: Technical Design Report*. CERN, Geneva, 1999. <http://cds.cern.ch/record/401974>.
- [50] ALICE Collaboration, *ALICE dimuon forward spectrometer: addendum to the Technical Design Report*. CERN, Geneva, 2000. <https://cds.cern.ch/record/494265>.
- [51] ALICE Collaboration, E. Abbas *et al.*, “Performance of the ALICE VZERO system”, *JINST* **8** (2013) P10016, arXiv:1306.3130 [nucl-ex].
- [52] ALICE Collaboration, B. Abelev *et al.*, “Measurement of the cross section for electromagnetic dissociation with neutron emission in Pb–Pb collisions at $\sqrt{s_{NN}} = 2.76$ TeV”, *Phys. Rev. Lett.* **109** (2012) 252302, arXiv:1203.2436 [nucl-ex].
- [53] ALICE Collaboration, F. Bossu *et al.*, “Performance of the RPC-based ALICE muon trigger system at the LHC”, *JINST* **7** (2012) T12002, arXiv:1211.1948 [physics.ins-det].
- [54] ALICE Collaboration, S. Acharya *et al.*, “Z-boson production in p-Pb collisions at $\sqrt{s_{NN}} = 8.16$ TeV and Pb–Pb collisions at $\sqrt{s_{NN}} = 5.02$ TeV”, *JHEP* **09** (2020) 076, arXiv:2005.11126 [nucl-ex].
- [55] ALICE Collaboration, “Centrality determination in heavy ion collisions”, ALICE-PUBLIC-2018-011. <https://cds.cern.ch/record/2636623>.
- [56] ALICE Collaboration, S. Acharya *et al.*, “Inclusive J/ψ production at mid-rapidity in pp collisions at $\sqrt{s} = 5.02$ TeV”, *JHEP* **10** (2019) 084, arXiv:1905.07211 [nucl-ex].
- [57] ALICE Collaboration, S. Acharya *et al.*, “Inclusive quarkonium production in pp collisions at $\sqrt{s} = 5.02$ TeV”, *Eur. Phys. J. C* **83** (2023) 61, arXiv:2109.15240 [nucl-ex].
- [58] F. Bossu, Z. C. del Valle, A. de Falco, M. Gagliardi, S. Grigoryan, and G. Martinez Garcia, “Phenomenological interpolation of the inclusive J/ψ cross section to proton-proton collisions at 2.76 TeV and 5.5 TeV”, arXiv:1103.2394 [nucl-ex].
- [59] ALICE Collaboration, “ J/ψ production at midrapidity in p–Pb collisions at $\sqrt{s_{NN}} = 8.16$ TeV”, arXiv:2211.14153 [nucl-ex].

- [60] ALICE Collaboration, “Quarkonium signal extraction in ALICE”, ALICE-PUBLIC-2015-006. <https://cds.cern.ch/record/2060096>.
- [61] ALICE Collaboration, S. Acharya *et al.*, “Energy dependence of forward-rapidity J/ψ and $\psi(2S)$ production in pp collisions at the LHC”, *Eur. Phys. J. C* **77** (2017) 392, arXiv:1702.00557 [hep-ex].
- [62] ALICE Collaboration, “ $\psi(2S)$ suppression in Pb-Pb collisions at the LHC”, arXiv:2210.08893 [nucl-ex].
- [63] X.-N. Wang and M. Gyulassy, “HIJING: A Monte Carlo model for multiple jet production in pp, pA and AA collisions”, *Phys. Rev.* **D44** (1991) 3501–3516.
- [64] T. Sjöstrand, S. Mrenna, and P. Skands, “A brief introduction to PYTHIA 8.1”, *Computer Physics Communications* **178** (2008) 852–867.
- [65] P. Golonka and Z. Was, “PHOTOS Monte Carlo: A Precision tool for QED corrections in Z and W decays”, *Eur. Phys. J.* **C45** (2006) 97, arXiv:hep-ph/0506026 [hep-ph].
- [66] ALICE Collaboration, S. Acharya *et al.*, “Measurement of the inclusive J/ψ polarization at forward rapidity in pp collisions at $\sqrt{s_{NN}} = 8$ TeV”, *Eur. Phys. J. C* **78** (2018) 562.
- [67] ALICE Collaboration, S. Acharya *et al.*, “First measurement of quarkonium polarization in nuclear collisions at the LHC”, *Phys. Lett. B* **815** (2021) 136146, arXiv:2005.11128 [nucl-ex].
- [68] R. Brun, F. Bruyant, M. Maire, A. C. McPherson, and P. Zancarini, *GEANT 3: user’s guide Geant 3.10, Geant 3.11; rev. version*. CERN, Geneva, 1987. <https://cds.cern.ch/record/1119728>.
- [69] ALICE Collaboration, S. Acharya *et al.*, “Inclusive J/ψ production at mid-rapidity in pp collisions at $\sqrt{s} = 5.02$ TeV”, *JHEP* **10** (2019) 084, arXiv:1905.07211 [nucl-ex].
- [70] X. Zhao and R. Rapp, “Transverse momentum spectra of J/ψ in heavy-ion collisions”, *Phys. Lett.* **B664** (2008) 253–257, arXiv:0712.2407 [hep-ph].
- [71] ALICE Collaboration, B. Abelev *et al.*, “Coherent J/ψ photoproduction in ultra-peripheral Pb–Pb collisions at $\sqrt{s_{NN}} = 2.76$ TeV”, *Phys. Lett. B* **718** (2013) 1273–1283, arXiv:1209.3715 [nucl-ex].
- [72] ALICE Collaboration, S. Acharya *et al.*, “Coherent J/ψ photoproduction at forward rapidity in ultra-peripheral Pb–Pb collisions at $\sqrt{s_{NN}} = 5.02$ TeV”, *Phys. Lett. B* **798** (2019) 134926, arXiv:1904.06272 [nucl-ex].
- [73] ALICE Collaboration, S. Acharya *et al.*, “Coherent J/ψ and ψ' photoproduction at midrapidity in ultra-peripheral Pb–Pb collisions at $\sqrt{s_{NN}} = 5.02$ TeV”, *Eur. Phys. J. C* **81** (2021) 712, arXiv:2101.04577 [nucl-ex].
- [74] ALICE Collaboration, J. Adam *et al.*, “Measurement of an excess in the yield of J/ψ at very low p_T in Pb–Pb collisions at $\sqrt{s_{NN}} = 2.76$ TeV”, *Phys. Rev. Lett.* **116** (2016) 222301, arXiv:1509.08802 [nucl-ex].
- [75] ALICE Collaboration, “Photoproduction of low- p_T J/ψ from peripheral to central Pb–Pb collisions at 5.02 TeV”, arXiv:2204.10684 [nucl-ex].
- [76] B. Wu, X. Du, M. Sibila, and R. Rapp, “ $X(3872)$ transport in heavy-ion collisions”, *Eur. Phys. J. A* **57** (2021) 122, arXiv:2006.09945 [nucl-th]. [Erratum: *Eur.Phys.J.A* 57, 314 (2021)].

- [77] B. Chen, “Thermal production of charmonia in Pb–Pb collisions at $\sqrt{s_{NN}} = 5.02$ TeV”, *Chin. Phys. C* **43** (2019) 124101, arXiv:1811.11393 [nucl-th].
- [78] L. Grandchamp and R. Rapp, “Thermal versus direct J/ψ production in ultrarelativistic heavy ion collisions”, *Phys. Lett. B* **523** (2001) 60–66, arXiv:hep-ph/0103124.
- [79] L. Grandchamp, R. Rapp, and G. E. Brown, “In medium effects on charmonium production in heavy ion collisions”, *Phys. Rev. Lett.* **92** (2004) 212301, arXiv:hep-ph/0306077.
- [80] X. Zhao and R. Rapp, “Charmonium in medium: from correlators to experiment”, *Phys. Rev. C* **82** (2010) 064905, arXiv:1008.5328 [hep-ph].
- [81] X. Zhao and R. Rapp, “Medium modifications and production of charmonia at LHC”, *Nucl. Phys. A* **859** (2011) 114–125, arXiv:1102.2194 [hep-ph].
- [82] E. Schnedermann, J. Sollfrank, and U. Heinz, “Thermal phenomenology of hadrons from 200A GeV S+S collisions”, *Phys. Rev. C* **48** (Nov, 1993) 2462–2475.
<https://link.aps.org/doi/10.1103/PhysRevC.48.2462>.
- [83] ALICE Collaboration, S. Acharya *et al.*, “Charm-quark fragmentation fractions and production cross section at midrapidity in pp collisions at the LHC”, *Phys. Rev. D* **105** (2022) L011103, arXiv:2105.06335 [nucl-ex].
- [84] K. J. Eskola, H. Paukkunen, and C. A. Salgado, “EPS09: A New Generation of NLO and LO Nuclear Parton Distribution Functions”, *JHEP* **04** (2009) 065, arXiv:0902.4154 [hep-ph].
- [85] ALICE Collaboration, S. Acharya *et al.*, “Prompt D^0 , D^+ , and D^{*+} production in Pb–Pb collisions at $\sqrt{s_{NN}} = 5.02$ TeV”, *JHEP* **01** (2022) 174, arXiv:2110.09420 [nucl-ex].
- [86] R. Baier, Y. L. Dokshitzer, A. H. Mueller, S. Peigné, and D. Schiff, “Radiative energy loss of high-energy quarks and gluons in a finite volume quark - gluon plasma”, *Nucl. Phys. B* **483** (1997) 291–320, arXiv:hep-ph/9607355.
- [87] R. Baier, Y. L. Dokshitzer, A. H. Mueller, S. Peigne, and D. Schiff, “Radiative energy loss and $p(T)$ broadening of high-energy partons in nuclei”, *Nucl. Phys. B* **484** (1997) 265–282, arXiv:hep-ph/9608322.
- [88] PHENIX Collaboration, A. Adare *et al.*, “Ground and excited charmonium state production in $p + p$ collisions at $\sqrt{s} = 200$ GeV”, *Phys. Rev. D* **85** (2012) 092004, arXiv:1105.1966 [hep-ex].
- [89] NA50 Collaboration, M. C. Abreu *et al.*, “Transverse momentum distributions of J/ψ , $\psi(2S)$, Drell-Yan and continuum dimuons produced in Pb–Pb interactions at the SPS”, *Phys. Lett.* **B499** (2001) 85–96.
- [90] B. Z. Kopeliovich, J. Nemchik, A. Schäfer, and A. V. Tarasov, “Cronin effect in hadron production off nuclei”, *Phys. Rev. Lett.* **88** (May, 2002) 232303.
<https://link.aps.org/doi/10.1103/PhysRevLett.88.232303>.
- [91] PHENIX Collaboration, A. Adare *et al.*, “ J/ψ Production in $\sqrt{s_{NN}} = 200$ -GeV Cu+Cu Collisions”, *Phys. Rev. Lett.* **101** (2008) 122301, arXiv:0801.0220 [nucl-ex].

F.U. Haider⁹², H. Hamagaki⁷⁷, A. Hamdi⁷⁵, M. Hamid⁶, Y. Han¹³⁹, B.G. Hanley¹³⁵,
R. Hannigan¹⁰⁹, J. Hansen⁷⁶, M.R. Haque¹³⁴, J.W. Harris¹³⁸, A. Harton⁹, H. Hassan⁸⁸,
D. Hatzifotiadou⁵¹, P. Hauer⁴³, L.B. Havener¹³⁸, S.T. Heckel⁹⁶, E. Hellbär⁹⁸, H. Helstrup³⁵,
M. Hemmer⁶⁴, T. Herman³⁶, G. Herrera Corral⁸, F. Herrmann¹³⁶, S. Herrmann¹²⁷, K.F. Hetland³⁵,
B. Heybeck⁶⁴, H. Hillemanns³³, B. Hippolyte¹²⁸, F.W. Hoffmann⁷⁰, B. Hofman⁵⁹, B. Hohlweger⁸⁵,
G.H. Hong¹³⁹, M. Horst⁹⁶, A. Horzyk², Y. Hou⁶, P. Hristov³³, C. Huang⁷³, C. Hughes¹²¹,
P. Huhn⁶⁴, L.M. Huhta¹¹⁶, T.J. Humanic⁸⁹, L.A. Husova¹³⁶, A. Hutson¹¹⁵, R. Ilkaev¹⁴¹, H. Ilyas¹⁴,
M. Inaba¹²⁴, G.M. Innocenti³³, M. Ippolitov¹⁴¹, A. Isakov⁸⁷, T. Isidori¹¹⁷, M.S. Islam¹⁰⁰,
M. Ivanov¹³, M. Ivanov⁹⁸, V. Ivanov¹⁴¹, K.E. Iversen⁷⁶, M. Jablonski², B. Jacak⁷⁵, N. Jacazio²⁶,
P.M. Jacobs⁷⁵, S. Jadlovská¹⁰⁷, J. Jadlovsky¹⁰⁷, S. Jaelani⁸³, C. Jahnke¹¹², M.J. Jakubowska¹³⁴,
M.A. Janik¹³⁴, T. Janson⁷⁰, M. Jercic⁹⁰, S. Ji¹⁷, S. Jia¹⁰, A.A.P. Jimenez⁶⁵, F. Jonas⁸⁸, J.M. Jowett^{33,98},
J. Jung⁶⁴, M. Jung⁶⁴, A. Junique³³, A. Jusko¹⁰¹, M.J. Kabus^{33,134}, J. Kaewjai¹⁰⁶,
P. Kalinak⁶⁰, A.S. Kalteyer⁹⁸, A. Kalweit³³, V. Kaplin¹⁴¹, A. Karasu Uysal⁷², D. Karatovic⁹⁰,
O. Karavichev¹⁴¹, T. Karavicheva¹⁴¹, P. Karczmarczyk¹³⁴, E. Karpechev¹⁴¹, U. Kebschull⁷⁰,
R. Keidel¹⁴⁰, D.L.D. Keijdener⁵⁹, M. Keil³³, B. Ketzer⁴³, S.S. Khade⁴⁸, A.M. Khan⁶, S. Khan¹⁶,
A. Khanzadeev¹⁴¹, Y. Kharlov¹⁴¹, A. Khatun¹¹⁷, A. Khuntia¹⁰⁸, M.B. Kidson¹¹⁴, B. Kileng³⁵,
B. Kim¹⁰⁵, C. Kim¹⁷, D.J. Kim¹¹⁶, E.J. Kim⁶⁹, J. Kim¹³⁹, J.S. Kim⁴¹, J. Kim⁵⁸, J. Kim⁶⁹,
M. Kim¹⁹, S. Kim¹⁸, T. Kim¹³⁹, K. Kimura⁹³, S. Kirsch⁶⁴, I. Kisel³⁹, S. Kiselev¹⁴¹, A. Kisiel¹³⁴,
J.P. Kitowski², J.L. Klay⁵, J. Klein³³, S. Klein⁷⁵, C. Klein-Bösing¹³⁶, M. Kleiner⁶⁴,
T. Klemenz⁹⁶, A. Kluge³³, A.G. Knospe¹¹⁵, C. Kobdaj¹⁰⁶, T. Kollegger⁹⁸, A. Kondratyev¹⁴²,
N. Kondratyeva¹⁴¹, E. Kondratyuk¹⁴¹, J. König⁶⁴, S.A. Königstorfer⁹⁶, P.J. Konopka³³,
G. Kornakov¹³⁴, S.D. Koryciak², A. Kotliarov⁸⁷, V. Kovalenko¹⁴¹, M. Kowalski¹⁰⁸,
V. Kozuharov³⁷, I. Králik⁶⁰, A. Kravčáková³⁸, L. Krcal^{33,39}, M. Krivda^{101,60}, F. Krizek⁸⁷,
K. Krizkova Gajdosova³³, M. Kroesen⁹⁵, M. Krüger⁶⁴, D.M. Krupova³⁶, E. Kryshen¹⁴¹,
V. Kučera⁵⁸, C. Kuhn¹²⁸, P.G. Kuijter⁸⁵, T. Kumaoka¹²⁴, D. Kumar¹³³, L. Kumar⁹¹, N. Kumar⁹¹,
S. Kumar³², S. Kundu³³, P. Kurashvili⁸⁰, A. Kurepin¹⁴¹, A.B. Kurepin¹⁴¹, A. Kuryakin¹⁴¹,
S. Kushpil⁸⁷, J. Kvapil¹⁰¹, M.J. Kweon⁵⁸, Y. Kwon¹³⁹, S.L. La Pointe³⁹, P. La Rocca²⁷,
A. Lakrathok¹⁰⁶, M. Lamanna³³, R. Langoy¹²⁰, P. Larionov³³, E. Laudi³³, L. Lautner^{33,96},
R. Lavicka¹⁰³, R. Lea^{132,55}, H. Lee¹⁰⁵, I. Legrand⁴⁶, G. Legras¹³⁶, J. Lehrbach³⁹, T.M. Lelek²,
R.C. Lemmon⁸⁶, I. León Monzón¹¹⁰, M.M. Lesch⁹⁶, E.D. Lesser¹⁹, P. Lévai¹³⁷, X. Li¹⁰, X.L. Li⁶,
J. Lien¹²⁰, R. Lietava¹⁰¹, I. Likmeta¹¹⁵, B. Lim²⁵, S.H. Lim¹⁷, V. Lindenstruth³⁹, A. Lindner⁴⁶,
C. Lippmann⁹⁸, A. Liu¹⁹, D.H. Liu⁶, J. Liu¹¹⁸, G.S.S. Liveraro¹¹², I.M. Lofnes²¹, C. Loizides⁸⁸,
S. Lokos¹⁰⁸, J. Lomker⁵⁹, P. Loncar³⁴, J.A. Lopez⁹⁵, X. Lopez¹²⁶, E. López Torres⁷, P. Lu^{98,119},
J.R. Luhder¹³⁶, M. Lunardon²⁸, G. Luparello⁵⁷, Y.G. Ma⁴⁰, M. Mager³³, A. Maire¹²⁸,
M.V. Makariev³⁷, M. Malaev¹⁴¹, G. Malfattore²⁶, N.M. Malik⁹², Q.W. Malik²⁰, S.K. Malik⁹²,
L. Malinina^{VI,142}, D. Mallick⁸¹, N. Mallick⁴⁸, G. Mandaglio^{31,53}, S.K. Mandal⁸⁰, V. Manko¹⁴¹,
F. Manso¹²⁶, V. Manzari⁵⁰, Y. Mao⁶, R.W. Marcjan², G.V. Margagliotti²⁴, A. Margotti⁵¹,
A. Marín⁹⁸, C. Markert¹⁰⁹, P. Martinengo³³, M.I. Martínez⁴⁵, G. Martínez García¹⁰⁴,
M.P.P. Martins¹¹¹, S. Masciocchi⁹⁸, M. Masera²⁵, A. Masoni⁵², L. Massacrier⁷³,
A. Mastroserio^{130,50}, O. Matonoha⁷⁶, S. Mattiazzo²⁸, P.F.T. Matuoka¹¹¹, A. Matyja¹⁰⁸, C. Mayer¹⁰⁸,
A.L. Mazuecos³³, F. Mazzaschi²⁵, M. Mazzilli³³, J.E. Mdhuli¹²², A.F. Mechler⁶⁴, Y. Melikyan^{44,141},
A. Menchaca-Rocha⁶⁷, E. Meninno^{103,29}, A.S. Menon¹¹⁵, M. Meres¹³, S. Mhlanga^{114,68}, Y. Miake¹²⁴,
L. Micheletti³³, L.C. Migliorin¹²⁷, D.L. Mihaylov⁹⁶, K. Mikhaylov^{142,141}, A.N. Mishra¹³⁷,
D. Miśkowiec⁹⁸, A. Modak⁴, A.P. Mohanty⁵⁹, B. Mohanty⁸¹, M. Mohisin Khan^{III,16},
M.A. Molander⁴⁴, Z. Moravcova⁸⁴, C. Mordasini⁹⁶, D.A. Moreira De Godoy¹³⁶, I. Morozov¹⁴¹,
A. Morsch³³, T. Mrnjavac³³, V. Muccifora⁴⁹, S. Muhuri¹³³, J.D. Mulligan⁷⁵, A. Mulliri²³,
M.G. Munhoz¹¹¹, R.H. Munzer⁶⁴, H. Murakami¹²³, S. Murray¹¹⁴, L. Musa³³, J. Musinsky⁶⁰,
J.W. Myrcha¹³⁴, B. Naik¹²², A.I. Nambrath¹⁹, B.K. Nandi⁴⁷, R. Nania⁵¹, E. Nappi⁵⁰,
A.F. Nassirpour^{18,76}, A. Nath⁹⁵, C. Nattrass¹²¹, M.N. Naydenov³⁷, A. Neagu²⁰, A. Negru¹²⁵,
L. Nellen⁶⁵, G. Neskovic³⁹, B.S. Nielsen⁸⁴, E.G. Nielsen⁸⁴, S. Nikolaev¹⁴¹, S. Nikulin¹⁴¹,
V. Nikulin¹⁴¹, F. Noferini⁵¹, S. Noh¹², P. Nomokonov¹⁴², J. Norman¹¹⁸, N. Novitzky¹²⁴,
P. Nowakowski¹³⁴, A. Nyanin¹⁴¹, J. Nystrand²¹, M. Ogino⁷⁷, A. Ohlson⁷⁶, V.A. Okorokov¹⁴¹,
J. Olińczak¹³⁴, A.C. Oliveira Da Silva¹²¹, M.H. Oliver¹³⁸, A. Onnerstad¹¹⁶, C. Oppedisano⁵⁶,
A. Ortiz Velasquez⁶⁵, J. Otwinowski¹⁰⁸, M. Oya⁹³, K. Oyama⁷⁷, Y. Pachmayer⁹⁵, S. Padhan⁴⁷,
D. Pagano^{132,55}, G. Paić⁶⁵, A. Palasciano⁵⁰, S. Panebianco¹²⁹, H. Park¹²⁴, H. Park¹⁰⁵, J. Park⁵⁸,
J.E. Parkkila³³, R.N. Patra⁹², B. Paul²³, H. Pei⁶, T. Peitzmann⁵⁹, X. Peng¹¹, M. Pennisi²⁵,

D. Peresunko¹⁴¹, G.M. Perez⁷, S. Perrin¹²⁹, Y. Pestov¹⁴¹, V. Petrov¹⁴¹, M. Petrovici⁴⁶,
 R.P. Pezzi^{104,66}, S. Piano⁵⁷, M. Pikna¹³, P. Pillot¹⁰⁴, O. Pinazza^{51,33}, L. Pinsky¹¹⁵, C. Pinto⁹⁶,
 S. Pisano⁴⁹, M. Płoskoń⁷⁵, M. Planinic⁹⁰, F. Pliquett⁶⁴, M.G. Poghosyan⁸⁸, B. Polichtchouk¹⁴¹,
 S. Politano³⁰, N. Poljak⁹⁰, A. Pop⁴⁶, S. Porteboeuf-Houssais¹²⁶, V. Pozdniakov¹⁴², I.Y. Pozos⁴⁵,
 K.K. Pradhan⁴⁸, S.K. Prasad⁴, S. Prasad⁴⁸, R. Preghenella⁵¹, F. Prino⁵⁶, C.A. Pruneau¹³⁵,
 I. Pshenichnov¹⁴¹, M. Puccio³³, S. Pucillo²⁵, Z. Pugelova¹⁰⁷, S. Qiu⁸⁵, L. Quaglia²⁵,
 R.E. Quishpe¹¹⁵, S. Ragoni¹⁵, A. Rakotozafindrabe¹²⁹, L. Ramello^{131,56}, F. Rami¹²⁸, S.A.R. Ramirez⁴⁵,
 T.A. Rancien⁷⁴, M. Rasa²⁷, S.S. Räsänen⁴⁴, R. Rath⁵¹, M.P. Rauch²¹, I. Ravasenga⁸⁵,
 K.F. Read^{88,121}, C. Reckziegel¹¹³, A.R. Redelbach³⁹, K. Redlich^{IV,80}, C.A. Reetz⁹⁸, A. Rehman²¹,
 F. Reidt³³, H.A. Reme-Ness³⁵, Z. Rescakova³⁸, K. Reygers⁹⁵, A. Riabov¹⁴¹, V. Riabov¹⁴¹,
 R. Ricci²⁹, M. Richter²⁰, A.A. Riedel⁹⁶, W. Riegler³³, C. Ristea⁶³, M.V. Rodriguez³³, M. Rodríguez
 Cahuantzi⁴⁵, K. Røed²⁰, R. Rogalev¹⁴¹, E. Rogochaya¹⁴², T.S. Rogoschinski⁶⁴, D. Rohr³³,
 D. Röhrich²¹, P.F. Rojas⁴⁵, S. Rojas Torres³⁶, P.S. Rokita¹³⁴, G. Romanenko¹⁴², F. Ronchetti⁴⁹,
 A. Rosano^{31,53}, E.D. Rosas⁶⁵, K. Roslon¹³⁴, A. Rossi⁵⁴, A. Roy⁴⁸, S. Roy⁴⁷, N. Rubini²⁶,
 O.V. Rueda¹¹⁵, D. Ruggiano¹³⁴, R. Rui²⁴, P.G. Russek², R. Russo⁸⁵, A. Rustamov⁸²,
 E. Ryabinkin¹⁴¹, Y. Ryabov¹⁴¹, A. Rybicki¹⁰⁸, H. Rytkonen¹¹⁶, J. Ryu¹⁷, W. Rzeska¹³⁴,
 O.A.M. Saarimaki⁴⁴, R. Sadek¹⁰⁴, S. Sadhu³², S. Sadovsky¹⁴¹, J. Saetre²¹, K. Šafařík³⁶, P. Saha⁴²,
 S.K. Saha⁴, S. Saha⁸¹, B. Sahoo⁴⁷, B. Sahoo⁴⁸, R. Sahoo⁴⁸, S. Sahoo⁶¹, D. Sahu⁴⁸, P.K. Sahu⁶¹,
 J. Saini¹³³, K. Sajdakova³⁸, S. Sakai¹²⁴, M.P. Salvan⁹⁸, S. Sambyal⁹², I. Sanna^{33,96}, T.B. Saramela¹¹¹,
 D. Sarkar¹³⁵, N. Sarkar¹³³, P. Sarma⁴², V. Sarritzu²³, V.M. Sarti⁹⁶, M.H.P. Sas¹³⁸, J. Schambach⁸⁸,
 H.S. Scheid⁶⁴, C. Schiaua⁴⁶, R. Schicker⁹⁵, A. Schmah⁹⁵, C. Schmidt⁹⁸, H.R. Schmidt⁹⁴,
 M.O. Schmidt³³, M. Schmidt⁹⁴, N.V. Schmidt⁸⁸, A.R. Schmier¹²¹, R. Schotter¹²⁸, A. Schröter³⁹,
 J. Schukraft³³, K. Schwarz⁹⁸, K. Schweda⁹⁸, G. Scioli²⁶, E. Scapparini⁵⁶, J.E. Seger¹⁵,
 Y. Sekiguchi¹²³, D. Sekihata¹²³, I. Selyuzhenkov⁹⁸, S. Senyukov¹²⁸, J.J. Seo⁵⁸, D. Serebryakov¹⁴¹,
 L. Šerkšnytė⁹⁶, A. Sevcenco⁶³, T.J. Shaba⁶⁸, A. Shabetai¹⁰⁴, R. Shahoyan³³, A. Shangaraev¹⁴¹,
 A. Sharma⁹¹, B. Sharma⁹², D. Sharma⁴⁷, H. Sharma^{54,108}, M. Sharma⁹², S. Sharma⁷⁷, S. Sharma⁹²,
 U. Sharma⁹², A. Shatat⁷³, O. Sheibani¹¹⁵, K. Shigaki⁹³, M. Shimomura⁷⁸, J. Shin¹², S. Shirinkin¹⁴¹,
 Q. Shou⁴⁰, Y. Sibiraki¹⁴¹, S. Siddhanta⁵², T. Siemiarczuk⁸⁰, T.F. Silva¹¹¹, D. Silvermyr⁷⁶,
 T. Simantathammakul¹⁰⁶, R. Simeonov³⁷, B. Singh⁹², B. Singh⁹⁶, K. Singh⁴⁸, R. Singh⁸¹, R. Singh⁹²,
 R. Singh⁴⁸, S. Singh¹⁶, V.K. Singh¹³³, V. Singhal¹³³, T. Sinha¹⁰⁰, B. Sitar¹³, M. Sitta^{131,56},
 T.B. Skaali²⁰, G. Skorodumovs⁹⁵, M. Slupecki⁴⁴, N. Smirnov¹³⁸, R.J.M. Snellings⁵⁹, E.H. Solheim²⁰,
 J. Song¹¹⁵, A. Songmoonak¹⁰⁶, C. Sonnabend^{33,98}, F. Soramel²⁸, A.B. Soto-hernandez⁸⁹, R. Spijkers⁸⁵,
 I. Sputowska¹⁰⁸, J. Staa⁷⁶, J. Stachel⁹⁵, I. Stan⁶³, P.J. Steffanic¹²¹, S.F. Stiefelmaier⁹⁵,
 D. Stocco¹⁰⁴, I. Storehaug²⁰, P. Stratmann¹³⁶, S. Strazzi²⁶, C.P. Stylianidis⁸⁵, A.A.P. Suaide¹¹¹,
 C. Suire⁷³, M. Sukhanov¹⁴¹, M. Suljic³³, R. Sultanov¹⁴¹, V. Sumberia⁹², S. Sumowidagdo⁸³,
 S. Swain⁶¹, I. Szarka¹³, M. Szymkowski¹³⁴, S.F. Taghavi⁹⁶, G. Taillepied⁹⁸, J. Takahashi¹¹²,
 G.J. Tambave⁸¹, S. Tang⁶, Z. Tang¹¹⁹, J.D. Tapia Takaki^{V,117}, N. Tapus¹²⁵, M.G. Tarzila⁴⁶,
 G.F. Tassielli³², A. Tauro³³, G. Tejada Muñoz⁴⁵, A. Telesca³³, L. Terlizzi²⁵, C. Terrevoli¹¹⁵,
 S. Thakur⁴, D. Thomas¹⁰⁹, A. Tikhonov¹⁴¹, A.R. Timmins¹¹⁵, M. Tkacik¹⁰⁷, T. Tkacik¹⁰⁷,
 A. Toia⁶⁴, R. Tokumoto⁹³, N. Topilskaya¹⁴¹, M. Toppi⁴⁹, T. Tork⁷³, A.G. Torres Ramos³²,
 A. Trifiró^{31,53}, A.S. Triolo^{33,31,53}, S. Tripathy⁵¹, T. Tripathy⁴⁷, S. Trogolo³³, V. Trubnikov³,
 W.H. Trzaska¹¹⁶, T.P. Trzcinski¹³⁴, A. Tumkin¹⁴¹, R. Turrisi⁵⁴, T.S. Tveter²⁰, K. Ullaland²¹,
 B. Ulukutlu⁹⁶, A. Uras¹²⁷, M. Urioni^{55,132}, G.L. Usai²³, M. Vala³⁸, N. Valle²², L.V.R. van
 Doremalen⁵⁹, M. van Leeuwen⁸⁵, C.A. van Veen⁹⁵, R.J.G. van Weelden⁸⁵, P. Vande Vyvre³³,
 D. Varga¹³⁷, Z. Varga¹³⁷, M. Vasileiou⁷⁹, A. Vasiliev¹⁴¹, O. Vázquez Doce⁴⁹, V. Vechernin¹⁴¹,
 E. Vercellin²⁵, S. Vergara Limón⁴⁵, L. Vermunt⁹⁸, R. Vértesi¹³⁷, M. Verweij⁵⁹, L. Vickovic³⁴,
 Z. Vilakazi¹²², O. Villalobos Baillie¹⁰¹, A. Villani²⁴, G. Vino⁵⁰, A. Vinogradov¹⁴¹, T. Virgili²⁹,
 M.M.O. Virta¹¹⁶, V. Vislavicius⁷⁶, A. Vodopyanov¹⁴², B. Volkel³³, M.A. Völkl⁹⁵, K. Voloshin¹⁴¹,
 S.A. Voloshin¹³⁵, G. Volpe³², B. von Haller³³, I. Vorobyev⁹⁶, N. Vozniuk¹⁴¹, J. Vrláková³⁸,
 J. Wan⁴⁰, C. Wang⁴⁰, D. Wang⁴⁰, Y. Wang⁴⁰, A. Wegrzynek³³, F.T. Weiglhofer³⁹, S.C. Wenzel³³,
 J.P. Wessels¹³⁶, S.L. Weyhmilller¹³⁸, J. Wiechula⁶⁴, J. Wikne²⁰, G. Wilk⁸⁰, J. Wilkinson⁹⁸,
 G.A. Willems¹³⁶, B. Windelband⁹⁵, M. Winn¹²⁹, J.R. Wright¹⁰⁹, W. Wu⁴⁰, Y. Wu¹¹⁹, R. Xu⁶,
 A. Yadav⁴³, A.K. Yadav¹³³, S. Yalcin⁷², Y. Yamaguchi⁹³, S. Yang²¹, S. Yano⁹³, Z. Yin⁶, I.-K. Yoo¹⁷,
 J.H. Yoon⁵⁸, H. Yu¹², S. Yuan²¹, A. Yuncu⁹⁵, V. Zaccolo²⁴, C. Zampolli³³, F. Zanone⁹⁵,
 N. Zardoshti³³, A. Zarochentsev¹⁴¹, P. Závada⁶², N. Zaviyalov¹⁴¹, M. Zhalov¹⁴¹, B. Zhang⁶,
 L. Zhang⁴⁰, S. Zhang⁴⁰, X. Zhang⁶, Y. Zhang¹¹⁹, Z. Zhang⁶, M. Zhao¹⁰, V. Zhrebchevskii¹⁴¹,

Y. Zhi¹⁰, D. Zhou⁶, Y. Zhou⁸⁴, J. Zhu^{98,6}, Y. Zhu⁶, S.C. Zugravel⁵⁶, N. Zurlo^{132,55}

Affiliation Notes

^I Deceased

^{II} Also at: Italian National Agency for New Technologies, Energy and Sustainable Economic Development (ENEA), Bologna, Italy

^{III} Also at: Department of Applied Physics, Aligarh Muslim University, Aligarh, India

^{IV} Also at: Institute of Theoretical Physics, University of Wroclaw, Poland

^V Also at: University of Kansas, Lawrence, Kansas, United States

^{VI} Also at: An institution covered by a cooperation agreement with CERN

Collaboration Institutes

¹ A.I. Alikhanyan National Science Laboratory (Yerevan Physics Institute) Foundation, Yerevan, Armenia

² AGH University of Science and Technology, Cracow, Poland

³ Bogolyubov Institute for Theoretical Physics, National Academy of Sciences of Ukraine, Kiev, Ukraine

⁴ Bose Institute, Department of Physics and Centre for Astroparticle Physics and Space Science (CAPSS), Kolkata, India

⁵ California Polytechnic State University, San Luis Obispo, California, United States

⁶ Central China Normal University, Wuhan, China

⁷ Centro de Aplicaciones Tecnológicas y Desarrollo Nuclear (CEADEN), Havana, Cuba

⁸ Centro de Investigación y de Estudios Avanzados (CINVESTAV), Mexico City and Mérida, Mexico

⁹ Chicago State University, Chicago, Illinois, United States

¹⁰ China Institute of Atomic Energy, Beijing, China

¹¹ China University of Geosciences, Wuhan, China

¹² Chungbuk National University, Cheongju, Republic of Korea

¹³ Comenius University Bratislava, Faculty of Mathematics, Physics and Informatics, Bratislava, Slovak Republic

¹⁴ COMSATS University Islamabad, Islamabad, Pakistan

¹⁵ Creighton University, Omaha, Nebraska, United States

¹⁶ Department of Physics, Aligarh Muslim University, Aligarh, India

¹⁷ Department of Physics, Pusan National University, Pusan, Republic of Korea

¹⁸ Department of Physics, Sejong University, Seoul, Republic of Korea

¹⁹ Department of Physics, University of California, Berkeley, California, United States

²⁰ Department of Physics, University of Oslo, Oslo, Norway

²¹ Department of Physics and Technology, University of Bergen, Bergen, Norway

²² Dipartimento di Fisica, Università di Pavia, Pavia, Italy

²³ Dipartimento di Fisica dell'Università and Sezione INFN, Cagliari, Italy

²⁴ Dipartimento di Fisica dell'Università and Sezione INFN, Trieste, Italy

²⁵ Dipartimento di Fisica dell'Università and Sezione INFN, Turin, Italy

²⁶ Dipartimento di Fisica e Astronomia dell'Università and Sezione INFN, Bologna, Italy

²⁷ Dipartimento di Fisica e Astronomia dell'Università and Sezione INFN, Catania, Italy

²⁸ Dipartimento di Fisica e Astronomia dell'Università and Sezione INFN, Padova, Italy

²⁹ Dipartimento di Fisica 'E.R. Caianiello' dell'Università and Gruppo Collegato INFN, Salerno, Italy

³⁰ Dipartimento DISAT del Politecnico and Sezione INFN, Turin, Italy

³¹ Dipartimento di Scienze MIFT, Università di Messina, Messina, Italy

³² Dipartimento Interateneo di Fisica 'M. Merlin' and Sezione INFN, Bari, Italy

³³ European Organization for Nuclear Research (CERN), Geneva, Switzerland

³⁴ Faculty of Electrical Engineering, Mechanical Engineering and Naval Architecture, University of Split, Split, Croatia

³⁵ Faculty of Engineering and Science, Western Norway University of Applied Sciences, Bergen, Norway

³⁶ Faculty of Nuclear Sciences and Physical Engineering, Czech Technical University in Prague, Prague, Czech Republic

³⁷ Faculty of Physics, Sofia University, Sofia, Bulgaria

³⁸ Faculty of Science, P.J. Šafárik University, Košice, Slovak Republic

³⁹ Frankfurt Institute for Advanced Studies, Johann Wolfgang Goethe-Universität Frankfurt, Frankfurt, Germany

- 40 Fudan University, Shanghai, China
41 Gangneung-Wonju National University, Gangneung, Republic of Korea
42 Gauhati University, Department of Physics, Guwahati, India
43 Helmholtz-Institut für Strahlen- und Kernphysik, Rheinische Friedrich-Wilhelms-Universität Bonn, Bonn, Germany
44 Helsinki Institute of Physics (HIP), Helsinki, Finland
45 High Energy Physics Group, Universidad Autónoma de Puebla, Puebla, Mexico
46 Horia Hulubei National Institute of Physics and Nuclear Engineering, Bucharest, Romania
47 Indian Institute of Technology Bombay (IIT), Mumbai, India
48 Indian Institute of Technology Indore, Indore, India
49 INFN, Laboratori Nazionali di Frascati, Frascati, Italy
50 INFN, Sezione di Bari, Bari, Italy
51 INFN, Sezione di Bologna, Bologna, Italy
52 INFN, Sezione di Cagliari, Cagliari, Italy
53 INFN, Sezione di Catania, Catania, Italy
54 INFN, Sezione di Padova, Padova, Italy
55 INFN, Sezione di Pavia, Pavia, Italy
56 INFN, Sezione di Torino, Turin, Italy
57 INFN, Sezione di Trieste, Trieste, Italy
58 Inha University, Incheon, Republic of Korea
59 Institute for Gravitational and Subatomic Physics (GRASP), Utrecht University/Nikhef, Utrecht, Netherlands
60 Institute of Experimental Physics, Slovak Academy of Sciences, Košice, Slovak Republic
61 Institute of Physics, Homi Bhabha National Institute, Bhubaneswar, India
62 Institute of Physics of the Czech Academy of Sciences, Prague, Czech Republic
63 Institute of Space Science (ISS), Bucharest, Romania
64 Institut für Kernphysik, Johann Wolfgang Goethe-Universität Frankfurt, Frankfurt, Germany
65 Instituto de Ciencias Nucleares, Universidad Nacional Autónoma de México, Mexico City, Mexico
66 Instituto de Física, Universidade Federal do Rio Grande do Sul (UFRGS), Porto Alegre, Brazil
67 Instituto de Física, Universidad Nacional Autónoma de México, Mexico City, Mexico
68 iThemba LABS, National Research Foundation, Somerset West, South Africa
69 Jeonbuk National University, Jeonju, Republic of Korea
70 Johann-Wolfgang-Goethe Universität Frankfurt Institut für Informatik, Fachbereich Informatik und Mathematik, Frankfurt, Germany
71 Korea Institute of Science and Technology Information, Daejeon, Republic of Korea
72 KTO Karatay University, Konya, Turkey
73 Laboratoire de Physique des 2 Infinis, Irène Joliot-Curie, Orsay, France
74 Laboratoire de Physique Subatomique et de Cosmologie, Université Grenoble-Alpes, CNRS-IN2P3, Grenoble, France
75 Lawrence Berkeley National Laboratory, Berkeley, California, United States
76 Lund University Department of Physics, Division of Particle Physics, Lund, Sweden
77 Nagasaki Institute of Applied Science, Nagasaki, Japan
78 Nara Women's University (NWU), Nara, Japan
79 National and Kapodistrian University of Athens, School of Science, Department of Physics, Athens, Greece
80 National Centre for Nuclear Research, Warsaw, Poland
81 National Institute of Science Education and Research, Homi Bhabha National Institute, Jatni, India
82 National Nuclear Research Center, Baku, Azerbaijan
83 National Research and Innovation Agency - BRIN, Jakarta, Indonesia
84 Niels Bohr Institute, University of Copenhagen, Copenhagen, Denmark
85 Nikhef, National institute for subatomic physics, Amsterdam, Netherlands
86 Nuclear Physics Group, STFC Daresbury Laboratory, Daresbury, United Kingdom
87 Nuclear Physics Institute of the Czech Academy of Sciences, Husinec-Řež, Czech Republic
88 Oak Ridge National Laboratory, Oak Ridge, Tennessee, United States
89 Ohio State University, Columbus, Ohio, United States
90 Physics department, Faculty of science, University of Zagreb, Zagreb, Croatia
91 Physics Department, Panjab University, Chandigarh, India
92 Physics Department, University of Jammu, Jammu, India

- ⁹³ Physics Program and International Institute for Sustainability with Knotted Chiral Meta Matter (SKCM2), Hiroshima University, Hiroshima, Japan
- ⁹⁴ Physikalisches Institut, Eberhard-Karls-Universität Tübingen, Tübingen, Germany
- ⁹⁵ Physikalisches Institut, Ruprecht-Karls-Universität Heidelberg, Heidelberg, Germany
- ⁹⁶ Physik Department, Technische Universität München, Munich, Germany
- ⁹⁷ Politecnico di Bari and Sezione INFN, Bari, Italy
- ⁹⁸ Research Division and ExtreMe Matter Institute EMMI, GSI Helmholtzzentrum für Schwerionenforschung GmbH, Darmstadt, Germany
- ⁹⁹ Saga University, Saga, Japan
- ¹⁰⁰ Saha Institute of Nuclear Physics, Homi Bhabha National Institute, Kolkata, India
- ¹⁰¹ School of Physics and Astronomy, University of Birmingham, Birmingham, United Kingdom
- ¹⁰² Sección Física, Departamento de Ciencias, Pontificia Universidad Católica del Perú, Lima, Peru
- ¹⁰³ Stefan Meyer Institut für Subatomare Physik (SMI), Vienna, Austria
- ¹⁰⁴ SUBATECH, IMT Atlantique, Nantes Université, CNRS-IN2P3, Nantes, France
- ¹⁰⁵ Sungkyunkwan University, Suwon City, Republic of Korea
- ¹⁰⁶ Suranaree University of Technology, Nakhon Ratchasima, Thailand
- ¹⁰⁷ Technical University of Košice, Košice, Slovak Republic
- ¹⁰⁸ The Henryk Niewodniczanski Institute of Nuclear Physics, Polish Academy of Sciences, Cracow, Poland
- ¹⁰⁹ The University of Texas at Austin, Austin, Texas, United States
- ¹¹⁰ Universidad Autónoma de Sinaloa, Culiacán, Mexico
- ¹¹¹ Universidade de São Paulo (USP), São Paulo, Brazil
- ¹¹² Universidade Estadual de Campinas (UNICAMP), Campinas, Brazil
- ¹¹³ Universidade Federal do ABC, Santo Andre, Brazil
- ¹¹⁴ University of Cape Town, Cape Town, South Africa
- ¹¹⁵ University of Houston, Houston, Texas, United States
- ¹¹⁶ University of Jyväskylä, Jyväskylä, Finland
- ¹¹⁷ University of Kansas, Lawrence, Kansas, United States
- ¹¹⁸ University of Liverpool, Liverpool, United Kingdom
- ¹¹⁹ University of Science and Technology of China, Hefei, China
- ¹²⁰ University of South-Eastern Norway, Kongsberg, Norway
- ¹²¹ University of Tennessee, Knoxville, Tennessee, United States
- ¹²² University of the Witwatersrand, Johannesburg, South Africa
- ¹²³ University of Tokyo, Tokyo, Japan
- ¹²⁴ University of Tsukuba, Tsukuba, Japan
- ¹²⁵ University Politehnica of Bucharest, Bucharest, Romania
- ¹²⁶ Université Clermont Auvergne, CNRS/IN2P3, LPC, Clermont-Ferrand, France
- ¹²⁷ Université de Lyon, CNRS/IN2P3, Institut de Physique des 2 Infinis de Lyon, Lyon, France
- ¹²⁸ Université de Strasbourg, CNRS, IPHC UMR 7178, F-67000 Strasbourg, France, Strasbourg, France
- ¹²⁹ Université Paris-Saclay Centre d'Etudes de Saclay (CEA), IRFU, Département de Physique Nucléaire (DPhN), Saclay, France
- ¹³⁰ Università degli Studi di Foggia, Foggia, Italy
- ¹³¹ Università del Piemonte Orientale, Vercelli, Italy
- ¹³² Università di Brescia, Brescia, Italy
- ¹³³ Variable Energy Cyclotron Centre, Homi Bhabha National Institute, Kolkata, India
- ¹³⁴ Warsaw University of Technology, Warsaw, Poland
- ¹³⁵ Wayne State University, Detroit, Michigan, United States
- ¹³⁶ Westfälische Wilhelms-Universität Münster, Institut für Kernphysik, Münster, Germany
- ¹³⁷ Wigner Research Centre for Physics, Budapest, Hungary
- ¹³⁸ Yale University, New Haven, Connecticut, United States
- ¹³⁹ Yonsei University, Seoul, Republic of Korea
- ¹⁴⁰ Zentrum für Technologie und Transfer (ZTT), Worms, Germany
- ¹⁴¹ Affiliated with an institute covered by a cooperation agreement with CERN
- ¹⁴² Affiliated with an international laboratory covered by a cooperation agreement with CERN.